

SUB-INERTIAL GRAVITY MODES IN THE B8V STAR KIC 7760680 REVEAL MODERATE CORE OVERSHOOTING AND LOW VERTICAL DIFFUSIVE MIXING

EHSAN MORAVVEJI¹

¹Institute of Astronomy, KU Leuven, Celestijnenlaan 200D, 3001 Leuven, Belgium

AND

RICHARD H. D. TOWNSEND²

²Department of Astronomy, University of Wisconsin-Madison, Madison, WI 53706, USA

AND

CONNY AERTS^{1,3}

³Department of Astrophysics, IMAPP, Radboud University Nijmegen, PO Box 9010, 6500 GL, Nijmegen, The Netherlands

AND

STÉPHANE MATHIS⁴

⁴Laboratoire AIM Paris-Saclay, CEA/DSM - CNRS - Université Paris Diderot, IRFU/SAP Centre de Saclay, 91191, Gif-sur-Yvette Cedex, France

Draft version November 6, 2018

ABSTRACT

KIC 7760680 is so far the richest slowly pulsating B star, by exhibiting 36 consecutive dipole ($\ell = 1$) gravity (g-) modes. The monotonically decreasing period spacing of the series, in addition to the local dips in the pattern confirm that KIC 7760680 is a moderate rotator, with clear mode trapping in chemically inhomogeneous layers. We employ the traditional approximation of rotation to incorporate rotational effects on g-mode frequencies. Our detailed forward asteroseismic modelling of this g-mode series reveals that KIC 7760680 is a moderately rotating B star with mass $\sim 3.25 M_{\odot}$. By simultaneously matching the slope of the period spacing, and the number of modes in the observed frequency range, we deduce that the equatorial rotation frequency of KIC 7760680 is 0.4805 day^{-1} , which is 26% of its Roche break up frequency. The relative deviation of the model frequencies and those observed is less than one percent. We succeed to tightly constrain the exponentially-decaying convective core overshooting parameter to $f_{\text{ov}} \approx 0.024 \pm 0.001$. This means that convective core overshooting can coexist with moderate rotation. Moreover, models with exponentially-decaying overshoot from the core outperform those with the classical step-function overshoot. The best value for extra diffusive mixing in the radiatively stable envelope is confined to $\log D_{\text{ext}} \approx 0.75 \pm 0.25$ (with D_{ext} in $\text{cm}^2 \text{sec}^{-1}$), which is notably smaller than theoretical predictions.

Keywords: asteroseismology, diffusion, waves, stars: interiors, stars: rotation, stars: individual (KIC 7760680)

1. INTRODUCTION

Late- to mid-type B stars have masses between ~ 3 to $7 M_{\odot}$, and are pulsationally unstable against low-degree high-order $|n_{\text{pg}}| \gtrsim 10$ g-modes, with periods ranging from ~ 0.5 to ~ 3 days. They are classified as slowly pulsating B (SPB) stars (Waelkens 1991; Waelkens et al. 1998; De Cat & Aerts 2002; Aerts et al. 2010). Non-adiabatic heat exchange around the iron opacity bump at $\log T \approx 5.2 \text{ K}$ – known as the classical κ –mechanism – is responsible for their mode excitation (Gautschy & Saio 1993; Dziembowski et al. 1993). Together with γ Dor stars, they are the richest main-sequence g-mode pulsators with numerous excited modes (e.g. Fig. 2e in Moravveji 2016). Chemically inhomogeneous regions above the receding convective cores reside inside this propagation cavity, and allow for partial or complete g-mode trapping, providing a unique physical diagnostic of the chemical mixing and thermal stratification in the deep stellar interior (Miglio et al. 2008; Cunha et al.

2015). In addition, g-modes can have sizeable amplitudes inside the narrow overshooting region – between the fully-mixed convective core and the μ -gradient layer, allowing to constrain the extent and physical properties of the overshooting layer (Dziembowski & Pamyatnykh 1991; Moravveji et al. 2015; Moravveji 2015). In such circumstances, g-modes can resolve and probe the physical conditions of the overshooting layer.

Moderate to rapid rotation is a fairly established property of (single and binary) SPB stars (Huang et al. 2010), and in general massive stars (Dufton et al. 2013; Ramírez-Agudelo et al. 2013, 2015). As soon as rotation kicks in, the centrifugal force deforms the star, and large-scale advection sets in. Then, the thermal and structural equilibrium of stars undergo a readjustment, in order to conserve mass, energy, linear and angular momentum (Kippenhahn & Thomas 1970; Endal & Sofia 1976, 1978; Zahn 1992; Maeder & Zahn 1998; Mathis & Zahn 2004; Maeder 2009; Espinosa Lara & Rieutord 2013). As a consequence of this, a handful of (advective and diffusive) mixing processes are triggered, smoothing chemical inhomogeneities in radiative envelopes and transferring

Electronic address: Ehsan.Moravveji@ster.kuleuven.be

¹ Marie Curie post-doctoral fellow.

angular momentum between the stellar core and envelope (see e.g. [Endal & Sofia 1978](#); [Heger et al. 2000, 2005](#); [Maeder 2009](#)). This poorly-known aspect of the theory of stellar evolution deserves a profound observational calibration. From observational and theoretical standpoints, however, there is a long way ahead to test and grasp all proposed mixing mechanisms, and the possible interplay between them ([Heger et al. 2000](#); [Maeder et al. 2013](#)). With asteroseismology of rotating and heat-driven pulsating stars, such as SPBs and γ Dor stars, we can quantitatively address several uncertain aspects of massive star evolution, and deep internal structure. The very slowly rotating pulsating *Kepler* B8V star KIC 10526294 ([Pápics et al. 2014](#), hereafter Star I) offered the first opportunity of seismic modelling of this type of pulsators. In [Moravveji et al. \(2015\)](#), we succeeded to place tight asteroseismic constraints on core overshooting, and extra diffusive mixing in the envelope of this star. That was followed by the derivation of its internal differential rotation profile by [Triana et al. \(2015\)](#), who inferred that the envelope of Star I rotates in the opposite direction with respect to its core.

Pulsation instability among late B-type stars is a known phenomenon from ground-based photometric and spectroscopic observations ([De Cat & Aerts 2002](#)), in addition to CoRoT and *Kepler* space photometry ([Pápics et al. 2011, 2012](#); [Balona et al. 2011](#)). The impact of rotation on pulsation modes is profound, and is thoroughly explained in the literature. For instance, [Unno et al. \(1989\)](#) and [Townsend \(2003a\)](#) explain different classes of heat-driven inertial pulsation modes that arise in rotating stars, like Rossby (r-) modes, Kelvin modes, and Yanai modes, because of the action of the Coriolis acceleration. The centrifugal deformation of the star affects the low-density outer envelope more significantly than the high-density core; thus, p-modes are more influenced by the centrifugal force, while g-modes are influenced by the Coriolis force ([Dintrans & Rieutord 2000](#); [Reese et al. 2006](#); [Ballot et al. 2010](#)). In addition to heat-driven modes destabilised by rotation, stochastic excitation of gravito-inertial waves was predicted by [Mathis et al. \(2014\)](#) and [Rogers et al. \(2013\)](#), and observed by [Neiner et al. \(2012\)](#) in the CoRoT B0IVe target HD 51452. The feedback from low-frequency g-modes and r-modes in SPB stars is efficient transport of angular momentum ([Rogers 2015](#); [Lee et al. 2014, 2016](#)). Nonradial pulsations are even proposed to cause the Be phenomena by the energy leakage of low-frequency prograde g-modes ([Shibahashi & Ishimatsu 2013](#)). This was already observed in B0.5IVe CoRoT target HD 49330 ([Huat et al. 2009](#)). Thus, rotation interacts profoundly with stellar structure, evolution and pulsation.

The pulsation description of rotating stars is at least a two-dimensional problem (e.g. [Prat et al. 2016](#)). However, it is possible to reduce this dimensionality into two separate one-dimensional problems for the radial ([Lee & Saio 1986](#)) and angular dependence ([Lee & Saio 1997](#); [Townsend 2003b](#)) of eigensolutions. That is achieved by ignoring the centrifugal deformation, and neglecting the horizontal component of the rotation vector in the momentum equation, when stratification dominates rotation (see e.g. the detailed discussion in [Mathis et al. 2008](#)). This is historically known as the Traditional Approximation of Rotation (TAR, [Eckart 1960](#)). Within the

TAR framework, [Townsend \(2005a,b\)](#) and [Aprilia et al. \(2011\)](#) have shown that the combination of buoyancy and Coriolis forces, when coupled with the κ -mechanism due to the iron-bump, provide a sufficient restoring force for driving high-order prograde $m = +1$ g-modes in SPB and γ Dor stars ([Savonije 2005](#); [Bouabid et al. 2013](#)). In addition, these modes are predicted to exhibit significant photometric light variability, and become observable ([Townsend 2003a](#); [Savonije 2013](#)).

The theoretical basis and observational facilities are now in place to exploit the wealth of information contained in the frequency spectrum of rotating pulsating B stars. The subject of this paper is the modelling and initial interpretation of a moderately rotating and slowly pulsating B8V star KIC 7760680 that was recently discovered by [Pápics et al. \(2015\)](#). We employ the identified series of dipole prograde g-modes in this star to address the following basic questions regarding the internal structure and global evolution of massive stars: (a) how to constrain the unknown rotation frequency of a rotating SPB star? (b) does rotation suppress core overshooting? (c) what are the combined and simultaneous effects of core overshoot mixing and additional mixing in the radiatively stable envelopes of B stars? (d) does the efficiency of the overshooting mixing decline radially from the fully mixed convective core, or does it stay strongly efficient over a fraction of scale heights away from the core boundary? Here, we provide answers to this set of questions, by a forward seismic modelling of our target star.

In Sect. 2 we introduce the seismic observables of KIC 7760680 that we exploit, and justify using traditional approximation when modelling high-order g-modes. The treatment of overshooting and extra diffusive mixing in the radiative envelope is the subject of Sect. 3, followed by introducing the input physics of four asteroseismic grids of non-rotating models in Sect. 4. The evolutionary models are computed with the one dimensional MESA stellar structure and evolution code ([Paxton et al. 2011, 2013](#); [Paxton et al. 2015](#), version 7678). The TAR and a comparison with first-order frequency perturbation are presented in Sect. 5. Our asteroseismic computations are performed with the GYRE (version 4.2) linear nonradial adiabatic/nonadiabatic one dimensional pulsation code ([Townsend & Teitler 2013](#)) that incorporates TAR. We introduce a simple and robust scheme to optimise the unknown rotation frequency of the star in Sect. 6, and statistically constrain the most likely rotation rate of the target. The meric function that we use for model selection is discussed in Sect. 7. In Sect. 8, we proceed to choose the best asteroseismic model that reproduces the observed slanted period spacing pattern, and elaborate on mode stability properties, and their efficient trapping in the overshooting region. In Sect. 9, we summarise our findings, and discuss the missing input physics from current state-of-the-art one-dimensional evolutionary models, which need to be incorporated in the (near) future.

2. ASTEROSEISMIC OBSERVABLES OF KIC 7760680

KIC 7760680 (B8 V) was observed by the nominal *Kepler* satellite for nearly four years. [Pápics et al. \(2015\)](#) carried out a thorough observational analysis of this target; below, we summarise their findings relevant to our

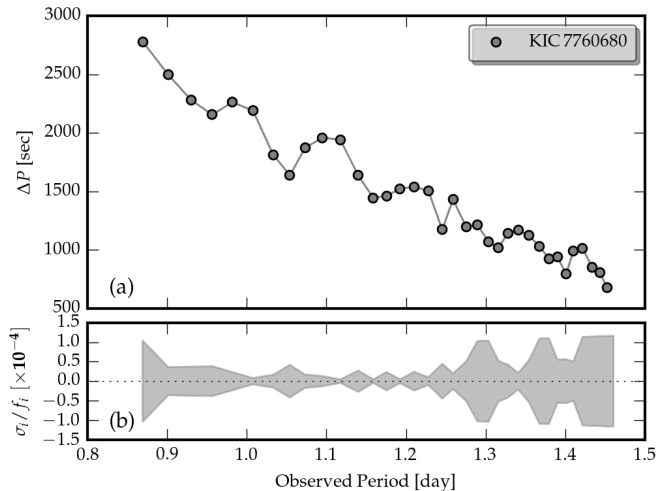


Figure 1. (a) The observed period spacing of KIC 7760680, consisting of 36 dipole prograde g-modes. For the list of observed modes refer to Table 1 in Pápics et al. (2015). The uncertainties are smaller than the plotting symbols. (b) The observed relative frequency uncertainty $\sigma_i/f_i^{(\text{obs})}$. Note that the ordinate is rescaled by a factor 10^{-4} for better visibility. The modes in the middle of the series have the highest precision.

modelling. The spectroscopic properties of KIC 7760680 from HERMES (Raskin et al. 2011) high-resolution spectra are $T_{\text{eff}} = 11650 \pm 210$ K, $\log g = 3.97 \pm 0.08$ dex, $[M/H] = 0.14 \pm 0.09$, and $v \sin i = 62 \pm 5$ km sec $^{-1}$. The inferred T_{eff} and $\log g$ places KIC 7760680 at the low-mass end of the SPB instability strip (Pamyatnykh 1999; Moravveji 2016).

Pápics et al. (2015) identified a series of $\mathcal{N} = 36$ low-frequency modes with periods between $P_1 \pm \sigma_1 = 0.86930 \pm 0.00002$ and $P_{36} \pm \sigma_{36} = 1.46046 \pm 0.00004$ days (their Table 1). This marks KIC 7760680 as the richest SPB, discovered so far. Fig. 1a shows the observed period spacing ΔP , and Fig. 1b shows the relative frequency uncertainty $\sigma_i/f_i^{(\text{obs})}$ around each mode. The striking feature of this series is the contiguous period spacing pattern with a negative slope. In a non-rotating star, the asymptotic period spacing is $\Delta P_{\ell}^{(\text{asy})} = 2\pi^2 \left(\sqrt{\ell(\ell+1)} \int_{r_0}^{r_1} N/r dr \right)^{-1}$, with r_0 and r_1 the inner and outer turning points of the mode propagation cavity, and the Brunt-Väisälä frequency N (Tassoul 1980). For a star with rotation frequency f_{rot} , and pulsation g-mode frequency $f_i^{(\text{co})}$ in the co-rotating frame, the spin parameter is defined as $s_i = 2f_{\text{rot}}/f_i^{(\text{co})}$, and the period spacing $\Delta P_{\ell,m}^{(\text{co})}(s)$ is

$$\Delta P_{\ell,m}^{(\text{co})}(s) \simeq \frac{2\pi^2}{\sqrt{\lambda_{\tilde{\ell},m,s(n+1)}} \int_{r_0}^{r_1} \frac{N}{r} dr \left(1 + \frac{1}{2} \frac{d \ln \lambda_{\tilde{\ell},m,s(n)}}{d \ln s} \right)}, \quad (1)$$

where $n, \tilde{\ell}, m$ are mode wavenumbers, and $\lambda_{\tilde{\ell},m,s}$ is the eigenvalue of the Laplace Tidal equation (Townsend 2003b; Ballot et al. 2012; Bouabid et al. 2013). For $f_{\text{rot}} = 0$, $\lambda_{\tilde{\ell},m,s}$ reduces to $\ell(\ell+1)$. Based on Eq. (1), period spacing depends sensitively on the thermal and chemical stratification through the Brunt-Väisälä frequency N , in addition to the star's rotation and pul-

sation frequencies through the spin parameter s . Thus, it provides a powerful asteroseismic diagnostic for constraining star's internal structure, in addition to its rotation frequency. Here, we attempt to model the observed pulsation frequencies, and reproduce the period spacing in Fig. 1a.

By a visual inspection of the observed period spacing pattern in Fig. 1a, two important inferences follow: (a) the negative moderate slope unravels the fact that KIC 7760680 is a moderate rotator. A comparison with Fig. 4 in Bouabid et al. (2013) and Figs. 4 & 5 in Van Reeth et al. (2015b) manifests that this series belongs to prograde modes, which are also theoretically predicted to be unstable in rotating SPB stars (Townsend 2005a,b; Aprilia et al. 2011). (b) there are clear deviations from the (tilted) asymptotic period spacing, which manifest themselves as local dips. The reason behind this is the presence of an additional bump in the Brunt-Väisälä frequency, associated with the μ -gradient zone above the core (Miglio et al. 2008), giving rise to efficient mode trapping in this region (discussed in Sect. 8.3). This inference was shown earlier after a detailed asteroseismic modelling of Star I (Fig. 2 in Moravveji 2015). This proves that the mixing in the radiative envelope is not strong enough to chemically homogenise the radiative zone. The presence of local dips in the observed period spacing puts an upper limit on the effective amount of chemical mixing in the radiative envelope of this rotating SPB.

The list of 36 dipole g-modes of KIC 7760680 were determined following the methodology discussed in detail in Degroote et al. (2009), which is based on the theory of time series analysis of correlated data (Schwarzenberg-Czerny 1991). Practically, we take the formal errors of the non-linear least-squares fit to the light curve, and correct them for the signal-to-noise ratio, sampling, and correlated nature of the data. Based on this procedure explained in Degroote et al., a correction factor of $Q = 4.0$ (P.I. Pápics, private communication) is applied to the formal errors listed in Table 1 of Pápics et al. (2015).

For heat-driven pulsators, unambiguous mode identification from (*Kepler*) white-light photometry is only possible if one detects (almost) equally-spaced frequency splittings around isolated peaks. Examples of such can be found in Pápics et al. (2014), Kurtz et al. (2014) and Saio et al. (2015). While this was feasible for Star I, Pápics et al. (2015) could not discern any frequency splitting for KIC 7760680, due to the very high density of peaks in the narrow g-mode frequency domain. Thus, one cannot assume any harmonic degree ℓ and azimuthal order m for the detected series. To tackle this, we computed few evolutionary tracks that pass through the 1σ position of the star on the Kiel diagram, and chose a model that closely reproduced the observed period spacing, after including rigid rotation. Then, we computed period spacing patterns for all possible combinations of $1 \leq \ell \leq 2$ and $|m| \leq \ell$ to explain the detected spacing. Appendix A and Fig. 11 present the results. The only possible way to simultaneously reproduce the slope of the observed series, the number of observed modes inside the observed range \mathcal{N} , and the location of the input model on the Kiel diagram (inside the 1σ spectroscopic box) is if the observed series be associated with dipole prograde $(\ell, m) = (1, +1)$ g-modes, which we adopt in

what follows.

3. A SIMPLIFIED MIXING SCHEME

Instead of exploiting non-exhaustive lists of proposed rotational and non-rotational mixing mechanisms (e.g. Heger et al. 2000, 2005; Maeder et al. 2013; Mathis 2013), we take a pragmatic approach and divide non-convective sources of mixing, and their corresponding coefficients into two distinct categories: (a) overshooting from the convective core into radiative interior in a diffusive regime D_{ov} , and (b) an effective extra diffusive mixing D_{ext} from top of the overshoot layer up to the surface. Hereafter, D_{ext} is in $\text{cm}^2 \text{sec}^{-1}$. Fig. 2a depicts our adopted mixing scheme. In the core, the convective mixing (blue) is computed from the Mixing Length Theory (MLT, Böhm-Vitense 1958; Cox & Giuli 1968); there, the temperature gradient is almost adiabatic $\nabla \simeq \nabla_{\text{ad}}$. The overshoot region (grey) is installed at the outer boundary of the convective core. MLT does not apply in this region, and D_{ov} is instead calculated from an ad hoc prescription. In the present work, we consider two prescriptions offered by MESA:

- A. Exponential overshoot (after Freytag et al. 1996; Herwig 2000), where the diffusion coefficient for overshoot has a radial dependence

$$D_{\text{ov}} = D_{\text{conv}} \exp\left(-\frac{2(r-r_0)}{f_{\text{ov}}H_p}\right) \quad r_0 \leq r. \quad (2)$$

Here, $r_0 = r_{\text{cc}} - f_0 H_p$ is the radial coordinate of the lower boundary of the overshoot region, which is situated at a depth $f_0 H_p$ below the radius r_{cc} of the convective core boundary; H_p is the pressure scale height, evaluated at r_{cc} , and D_{conv} is the convective mixing diffusion coefficient, evaluated from MLT at r_0 . The dimensionless parameters f_0 and f_{ov} allow tuning of the position and exponential scale, respectively, of the overshoot region. We fix $f_0 = 10^{-3}$ throughout the present work, but allow f_{ov} to vary.

- B. Step overshoot, where the diffusion coefficient for overshoot has a fixed value

$$D_{\text{ov}} = D_{\text{conv}} \quad r_0 \leq r \leq r_0 + \alpha_{\text{ov}} H_p. \quad (3)$$

The interpretations of r_0 , H_p and D_{conv} are the same as before, and again we adopt $f_0 = 10^{-3}$ throughout; but now the parameter α_{ov} tunes the extent of the overshooting zone.

In the overshoot region, MESA assumes $\nabla = \nabla_{\text{rad}}$; this differs from penetrative overshoot treatments (e.g. Roxburgh 1965; Maeder 1975; Zahn 1991; Viallet et al. 2015), which are similar to the step prescription B (above) but assume $\nabla = \nabla_{\text{ad}}$ over d_p a penetration distance derived in Zahn (1991). The time dependent turbulent convection model of Zhang (2016) allows to set ∇ between ∇_{ad} and ∇_{rad} , but those models are not confronted with observations, yet.

In Figs. 2b and 2c, we present the exponentially decaying and step-function prescriptions, respectively. The two best seismic models of our target (discussed later in Sect. 8.1) are used as input. For the former, the transition from overshoot to extra mixing in the envelope is

smooth. On the other hand, the step-function overshoot mixing, as in Fig. 2b implies constant mixing inside the overshoot zone, and suddenly drops by ~ 13 to 7 orders of magnitude, depending on what we adopt for D_{ext} . Here, the transition from overshoot to extra mixing is not smooth. The resulting Brunt-Väisälä frequencies N^2 are shown in both panels with red dashed lines. The difference between the two adopted overshoot prescriptions is that in the case of step-function overshoot, N^2 rises steeply at the top of the overshoot layer, whereas in the exponentially decaying model, N^2 grows smoothly. These two different N^2 profiles result in two different period spacing patterns, and allow discriminating them when modelling SPB stars.

Finally, a constant extra diffusive mixing (green hatch) is applied above the overshooting region across the remaining part of the radiative envelope (with $\nabla = \nabla_{\text{rad}}$, see Fig. 2). The extra mixing can be associated with advecto-diffusive mixing due to rotation instability (Heger et al. 2000; Maeder 2009), mixing by an internal magnetic field (Heger et al. 2005; Mathis & Zahn 2005), semi-convective mixing (Langer et al. 1985), internal gravity waves Talon & Charbonnel (2005); Pantiillon et al. (2007); Rogers et al. (2013); Rogers (2015), and other possible sources including their complex interaction (e.g. Maeder et al. 2013). Our proposed scheme is the least model-dependent approach to quantify the order-of-magnitude of the non-convective (diffusive) mixing coefficients beyond the fully mixed core in B stars.

Because both D_{ov} and D_{ext} are unconstrained from first principles, we parametrize them, and scan the parameter space to find the optimal values that explain the observed pulsation frequencies (or equivalently period spacing) of our target. We recently developed this approach in Moravveji et al. (2015), and carried out a detailed forward modelling of nineteen dipole ($\ell = 1$) g-modes in Star I (B8 V, $v \sin i < 18 \text{ km sec}^{-1}$). For this specific star, we found the diffusive exponential overshooting prescription more favorable than the step-function prescription, and confined the free overshooting parameter to $f_{\text{ov}} \approx 0.017$. Moreover, including extra diffusive mixing with coefficient of $\log D_{\text{ext}} = 1.75$ improved the quality of frequency fitting by a factor ~ 11 . This was the first asteroseismic quantification of extra mixing in B stars. Here, we apply the same methodology to KIC 7760680, which rotates much faster than Star I.

4. ASTEROSEISMIC MODELS

We compute non-rotating non-magnetic stellar structure and evolution models with MESA with the mixing scheme described in Sect. 3. Each evolutionary track is specified with the following three parameters at zero-age main sequence: the initial mass M_{ini} , core overshooting free parameter f_{ov} (for exponential overshoot) or α_{ov} (for step-function overshoot), and extra diffusive mixing beyond the overshoot region D_{ext} . All models assume the Asplund et al. (2009) metal mixture with the initial hydrogen mass fraction $X_{\text{ini}} = 0.71$ taken from the Galactic B-star standard of Nieva & Przybilla (2012). We vary the initial metallicity $Z_{\text{ini}} \in [0.014, 0.023]$; the initial helium abundance is then fixed accordingly $Y_{\text{ini}} = 1 - X_{\text{ini}} - Z_{\text{ini}}$. Along every evolutionary track, we store an equilibrium model at every ~ 0.001 drop in X_{c} . We terminate the evolution as soon as X_{c} drops below 10^{-3} . The

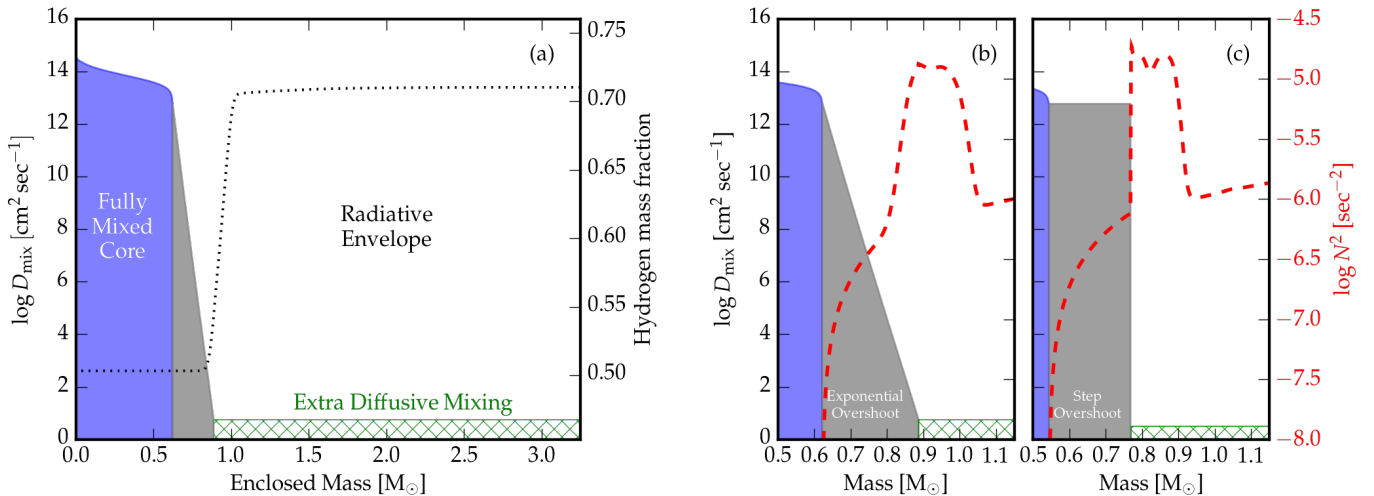


Figure 2. (a) The simplified mixing scheme in our evolutionary models, shown for the best asteroseismic model of KIC 7760680 (discussed in Sect. 8.1 and Table 2). The abscissa is the mass coordinate, and the ordinate is the logarithm of the mixing coefficient. The convective and overshooting regions are shown in blue and grey, respectively. Beyond the overshooting region, we include an additional diffusive mixing with varying strength, (green hatch). The profile of hydrogen mass fraction (dotted lines) shows that the overshoot region is fully mixed. (b) A zoom-in view around the overshoot region, for the best model with exponentially decaying prescription (Eq. 2). Grid A is built on this option. (c) Similarly, for the best model with step-function overshooting. Grid B is built on this option. Notice the difference between the two Brunt-Väisälä profiles (red dashed line), and the extent of the two mixing regions.

convective boundaries are specified using the Ledoux criterion. For the surface boundary condition, we use ATLAS9 tables of Castelli & Kurucz (2003) with surface optical depth $\tau_s = 2/3$. We include the line-driven mass loss prescription of Vink et al. (2001) with the efficiency factor reduced by a factor 3 (Puls et al. 2015).

Recently, Moravveji (2016) showed that a 75% increase in Iron and Nickel monochromatic opacities explains the position of two confirmed β Cep and eight confirmed hybrids on the Kiel diagram, which could not be explained before. The increase resulted from the direct laboratory Iron opacity measurement of Bailey et al. (2015), which was later confirmed by numerical simulations of Nagayama et al. (2016). We use this set of OP Iron- and Nickel-enhanced opacity tables, because it solves the pulsation instability problem in massive stars, in agreement with previous predictions (Dziembowski & Pamyatnykh 2008; Salmon et al. 2012). The recent OPAS opacity computation of Mondet et al. (2015) independently shows that the iron opacity is underestimated in default OP (Seaton 2005; Badnell et al. 2005) tables by $\sim 40\%$ (their discussion in Sect. 5). Our computations are based on a 75% Fe and Ni enhanced opacity tables. The MESA inlists, and the opacity tables are freely available for download. More information is provided in Appendix B.

Based on the above setup, we compute two evolutionary grids, with the range and stepsize of parameters listed in Table 1. The procedure is to start from a coarse parameter space, and iteratively zoom around the best parameter ranges by decreasing the parameter stepsize. The physical setup of both grids are identical, except for the choice of overshoot prescription. The exponential prescription is employed in grid A, where we vary f_{ov} (see Fig. 2b); similarly, the step-function prescription is used in grid B, where we vary α_{ov} (see Fig. 2c). This allows to assess which of the two overshooting prescriptions is superior, in the sense of providing a better fit to the observed frequencies. For Star I, we demonstrated that the exponential prescription outperformed the step-function

Table 1

Parameters of the two asteroseismic grids for KIC 7760680. We vary the initial mass M_{ini} , exponential (or step-function) overshoot f_{ov} (or α_{ov}), initial metallicity Z_{ini} , extra diffusive mixing $\log D_{\text{ext}}$ (in $\text{cm}^2 \text{sec}^{-1}$), and core hydrogen mass fraction (X_c). N is the total number of values for each parameter. The number of degrees of freedom for all grids is $n = 5$. “Step” gives the minimum stepsize in the corresponding parameter.

Grid	From	To	Step	N
A				
$M_{\text{ini}} [M_{\odot}]$	3.00	3.60	0.05	13
f_{ov}	0.007	0.031	≥ 0.001	13
Z_{ini}	0.014	0.023	≥ 0.001	8
$\log D_{\text{ext}}$	None	5.0	≥ 0.25	13
X_c	0.70	0.30	≥ 0.001	~ 401
B				
$M_{\text{ini}} [M_{\odot}]$	3.00	3.40	0.05	9
α_{ov}	0.21	0.33	≥ 0.01	9
Z_{ini}	0.014	0.023	≥ 0.001	4
$\log D_{\text{ext}}$	None	1.50	≥ 0.25	4
X_c	0.60	0.40	≥ 0.001	~ 201

one (Moravveji et al. 2015).

Extra diffusive mixing is one of the grid parameters that we vary from $\log D_{\text{ext}} = 0.25$ to 5.0. We also include models suppressing this; these are presented in Table 1 and the forthcoming figures with “None”. With this choice, we can examine if extra diffusive mixing is required in the envelope of SPB stars. For Star I, the χ^2 scores were reduced by a factor of more than 11 when we included extra mixing. Here, we re-examine this for KIC 7760680.

5. TRADITIONAL APPROXIMATION VERSUS FIRST-ORDER PERTURBATIONS

There are two possible approaches to incorporate the effect of rotation on pulsation frequencies based on 1D stellar models: one is through first-, second- and third-order perturbative methods (Ledoux 1951; Dziembowski & Goode 1992; Soufi et al. 1998), and the other is through

TAR. To assess the validity of the first-order perturbative approach (Ledoux 1951) versus the TAR, one should consider the spin parameter s . Ballot et al. (2010) showed that for p-modes and low-order g-modes, it is still possible to use first-, second-, and/or third-order frequency corrections to reproduce the results from TAR, for low values of the spin parameter $s \ll 1$ (refer to Bouabid et al. 2013, for γ Dor stars). As soon as $s_i \gtrsim 1$, the frequency splittings from perturbative methods depart from their counterparts within the TAR framework, due to ignoring the impact of the Coriolis force on pulsation frequencies. This is the case for high-order g-modes – even in slowly rotating stars – due to their small frequency values.

To demonstrate this, Fig. 3a compares periods of dipole prograde modes from the first-order perturbative method (open circles) versus those from TAR (red dots), in the observer (inertial) reference frame. The spin parameter for the corresponding modes in the co-rotating frame is shown in Fig. 3b. The input model corresponds to the best asteroseismic model of KIC 7760680 (to be discussed later in Sect. 8), and is set to rotate rigidly at 26.4% of the Roche break up frequency. The range of the observed modes is shown by the blue band. The difference between the two sets of periods is considerable, and the resulting period spacing – which is tangent to each of these curves – will significantly differ. For sub-inertial waves, the wave dynamics is modified compared to TAR computations (Mathis et al. 2008, 2014); however, Ballot et al. (2012) have shown that the resulting period spacing within TAR gives a correct prediction up to high spin parameters. Consequently, even for sub-inertial g-modes $s > 1$, we decided to employ the TAR.

Even though the centrifugal force implies deviations from spherical symmetry, this effect becomes important for stars rotating more than half critical (Fig. 1 in Aerts et al. 2004). Using Eqs. 1 and 2 in Aerts et al. (2004), the polar radius of our target is smaller than its equatorial radius by only $\sim 1.6\%$, when the star is set to rotate at 26% Roche critical frequency. Moreover, the stellar surface of slower rotators can deform significantly due to the effect of centrifugal force, the deep interior – where high-order g-modes propagate with larger amplitudes – departs negligibly from spherical symmetry; see e.g. Saio & Deupree (2012) for a demonstration. This means that modelling and studying the structure of the core overshooting layer in slow to moderate rotators with high-order g-modes, using one-dimensional stellar structure models coupled with one-dimensional oscillation theory under TAR, and ignoring the centrifugal deformation is fully justified.

6. OPTIMIZING ROTATION FREQUENCY

The lack of prior knowledge on the inclination angle of the rotation axis of our target precludes deducing the equatorial rotation frequency f_{rot} from the spectroscopic measurement of the projected rotation velocity $v \sin i = 2\pi R_* f_{\text{rot}} \sin i = 62 \pm 5 \text{ km sec}^{-1}$, assuming a reasonable radius R_* from models. Thus, f_{rot} is an additional unknown of KIC 7760680. Because MESA supports shellular rotation (Paxton et al. 2013), f_{rot} could be treated as another free parameter in our grids. However, we choose not to do so, because, through their dependence on the spin parameter s_i , the g-mode frequencies are very sensitive to even a slight change in f_{rot} in the

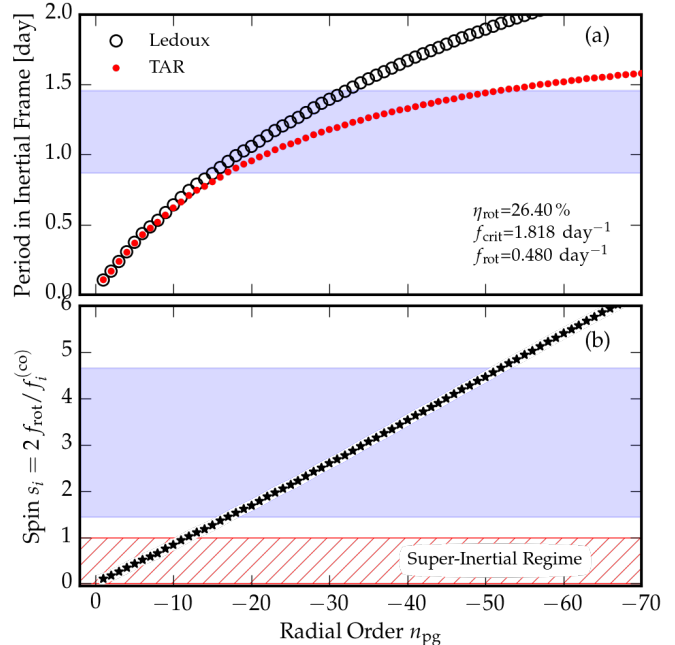


Figure 3. Top. First order perturbative periods (empty circles) versus those computed within TAR (red dots) in the inertial frame. The blue band highlights the observed period range of KIC 7760680. The equilibrium structure of the model is adapted to the best asteroseismic model of KIC 7760680 (Sect. 8), and is set to rotate rigidly at 26.4% of the Roche critical frequency. Bottom. The spin parameter for the corresponding mode frequencies in the co-rotating frame, $f_i^{(\text{co})}$. The observed modes (in blue band) fall outside the super-inertial regime $s \leq 1$ (red hatch), and lie in the sub-inertial regime $s > 1$.

co-rotating and inertial frames. As a demonstration, see Fig. 2 in Townsend (2005a) or Fig. 1.1 and 2 in Bouabid et al. (2013). This would require an unreasonably broad and immensely resolved parameter survey for f_{rot} , which is not computationally feasible. Instead we take a pragmatic approach, and optimise f_{rot} for every input model. One can benefit from the observational fact that there are exactly $\mathcal{N} = 36$ observed modes between f_1 and f_{36} (allowing for a tolerance around them). Thanks to the high sensitivity of \mathcal{N} to f_{rot} , we can tune the latter until $\mathcal{N} = 36$ is satisfied.

Fig. 4b shows the evolution of mode periods in the inertial frame versus rotation frequency f_{rot} . The blue band highlights the observed range. Clearly, increasing the rotation frequency (and hence the spin parameter) progressively increases the number of modes inside the observed range. At the same time few modes gradually leave the observed range. The net number of modes inside the observed range \mathcal{M} is shown in Fig. 4a, showing the strong dependence of \mathcal{M} on f_{rot} . The dashed horizontal line also shows the observed number of modes for KIC 7760680, i.e. $\mathcal{N} = 36$. We define $d\mathcal{N}(f_{\text{rot}})$ as an integer-valued function that captures the difference between the model and observed number of modes in the inertial frame within the observed range.

$$d\mathcal{N}(f_{\text{rot}}) = \mathcal{M} - \mathcal{N}, \quad (4)$$

Consequently, $d\mathcal{N}$ can be used as a discriminant to *optimize* the rotation frequency, for every input model from our grids, by seeking its root. Once the optimal rotation

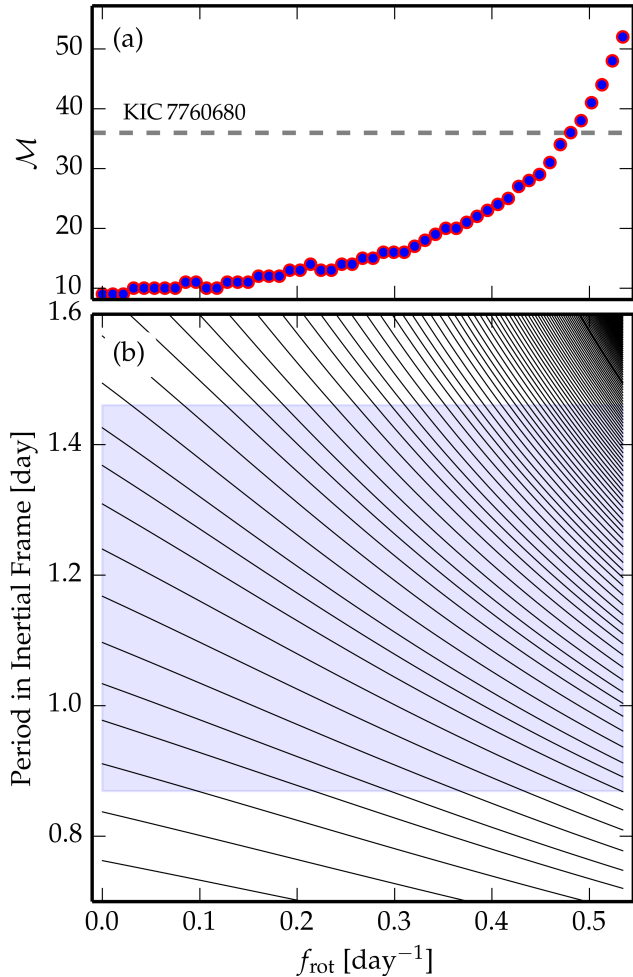


Figure 4. Top. The number of modes (circles) between the observed range (dashed line) \mathcal{N} versus rotation frequency f_{rot} in the inertial frame. Bottom. Evolution of the mode periods in the inertial frame $P_i^{(\text{in})}$ versus f_{rot} , for dipole prograde modes. We use the best model (Sect. 8.1 and Table 2) as input. The observed range $P_1 \leq P_i^{(\text{in})} \leq P_{36}$ is highlighted in blue. For higher f_{rot} , a dense spectrum of high-order g-modes enters the observed range from the top, rapidly increasing \mathcal{M} .

frequency $f_{\text{rot}}^{(\text{opt})}$ is located, then

$$\mathcal{M} = \mathcal{N}, \quad \text{for } f_{\text{rot}} = f_{\text{rot}}^{(\text{opt})}. \quad (5)$$

A brief description of the algorithm that locates the root of $d\mathcal{N}$ is given in the Appendix C. Although we started from non-rotating models, we can optimise the rotation frequency, assuming rigid rotation. Since our proposed algorithm has minimum underlying assumptions, we propose that it can be applied to any slow to moderately rotating star, including the *Kepler* sample of γ Dor stars of Van Reeth et al. (2015a,b), provided that we limit the study to the prograde and/or zonal modes.

Fig. 5 shows the histogram of the optimised rotation frequency for all models in grid A, which can be interpreted as the probability distribution function (PDF) of f_{rot} by requiring all models to fulfil Eq. (5). The PDF exhibits a skewed distribution, strongly deviating from a Gaussian distribution. The striking result of our optimisation scheme – reflected in the PDF – is that the $f_{\text{rot}}^{(\text{opt})}$ for 99% of the models lies between 0.4568

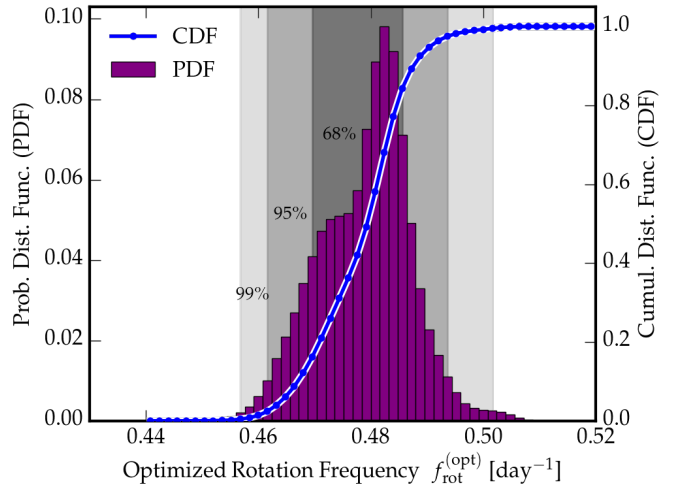


Figure 5. Histogram of the rotation frequency in grid A after rotation optimisation $f_{\text{rot}}^{(\text{opt})}$ (see Eq. 5). The blue curve is the cumulative distribution function (CDF) of the rotation frequency. The three shaded zones correspond to the rotation ranges where 99%, 95% and 68% of $f_{\text{rot}}^{(\text{opt})}$ lie, respectively.

to 0.5016 day^{-1} , which is already a tight constraint on the possible rotation frequency of the target. Similarly 68% of rotation frequencies lie between 0.4696 to 0.4856 day^{-1} . The mean optimised rotation frequency $\langle f_{\text{rot}} \rangle$ is simply a weighted average of optimised rotation frequencies $f_{\text{rot},k}^{(\text{opt})}$ within each histogram bin k , with the PDF within the same bin used as the weight w_k . In other words,

$$\langle f_{\text{rot}} \rangle = \frac{\sum_k w_k f_{\text{rot},k}^{(\text{opt})}}{\sum_k w_k}. \quad (6)$$

Together with the 1σ PDF range, the mean optimised rotation frequency of KIC 7760680 is $\langle f_{\text{rot}} \rangle = 0.4790^{+0.0066}_{-0.0094} \text{ day}^{-1}$.

At the end of this step, we append $f_{\text{rot}}^{(\text{opt})}$ to every model in our grids, ensuring that they reproduce the slope of the observed period spacing, and fulfil Eq. (4). Now, we can proceed to compute the χ^2 goodness-of-fit scores (next section) to rank all our input models accordingly.

7. MODEL FREQUENCIES AND RANKING

Each equilibrium structure model from our grids is fed into the adiabatic linear nonradial pulsation code GYRE, using TAR. We compute dipole prograde frequencies within a broad trial range that ensures covering the observed period range. In GYRE, the frequencies are internally computed in the co-rotating frame $f_i^{(\text{co})}$, for a trial rotation frequency $\omega_{\text{rot}} = 2\pi f_{\text{rot}}$, but are stored in the inertial frame $f_i^{(\text{in})}$, considering the Doppler shift $f_i^{(\text{in})} = f_i^{(\text{co})} + m f_{\text{rot}}$. This facilitates consistent comparison between the frequencies, periods and/or period spacings from observation and models.

Because we optimise the rotation frequency (Sect. 6), we can proceed to a mode-by-mode comparison between observations and models. To rank all models based on their quality of fitting the observed frequencies (Table 1 Pápics et al. 2015), we define a frequentist reduced- χ^2

score, denoted by χ_{red}^2

$$\chi_{\text{red}}^2 = \frac{1}{\mathcal{N} - n} \sum_{i=1}^{\mathcal{N}} \left(\frac{f_i^{(\text{obs})} - f_i^{(\text{mod})}}{\sigma_i} \right)^2. \quad (7)$$

where $\mathcal{N} = 36$ is the number of observed modes, $n = 5$ is the number of free parameters in each grid for the fixed input physics, and the σ_i are the 1σ uncertainties of observed frequencies. Consequently, we sort and tabulate all input models based on their associated χ_{red}^2 . Based on this, we pick the two best model(s), one from grid A, and the other from grid B, with minimum χ_{red}^2 scores. The properties of these models are discussed in Sect. 8.

8. RESULTS

8.1. Best Asteroseismic Model Candidates

Panels (a) to (e) in Fig. 6 show the distribution of the logarithm of χ_{red}^2 versus the free parameters of grid A. The ordinate is limited to the lowest χ_{red}^2 values, despite $\chi_{\text{red}}^2 \in [1808, 2.11 \times 10^8]$. The $\log \chi_{\text{red}}^2$ shows significant minima for most of the grid parameters, allowing to tightly constrain them. Our best asteroseismic model corresponds to the one that has the minimum χ_{red}^2 within each grid. In what follows, we call the best model from grid A as mA, and that of grid B as mB. The internal structure of model mA is freely available for download, as explained in Appendix B. Figs. 2b and 2c depict the internal structures of these two best models. Table 2 gives an overview of the physical properties of mA and mB that we elaborate below.

The large χ_{red}^2 values in Fig. 6 is a common situation when modelling heat-driven modes with such high precision frequencies. In spite of that, the most plausible parameters of KIC 7760680 are the following. The initial mass is roughly $M_{\text{ini}} = 3.25 M_{\odot}$, which is identical to that of Star I. Thus, KIC 7760680 is a moderately rotating analog of Star I. There is a clear indication that $Z_{\text{ini}} \approx 0.020$, which agrees with the spectroscopic estimate that $[M/H] = 0.14 \pm 0.09$. Thus, KIC 7760680 is a metal-rich dwarf. From Fig. 6e, the age is well-constrained to $X_c = 0.50$, implying that KIC 7760680 is still in its early main sequence evolution. The best value for the exponential overshooting parameter is $f_{\text{ov}} = 0.024$, although $f_{\text{ov}} \in [0.022, 0.026]$ result in comparatively good fits to the observed period spacing. Thus, the overshooting is stronger in this target, compared to that of the slower rotator Star I.

The extra diffusive mixing exhibits a distinct minimum around $\log D_{\text{ext}} \approx 0.75$. Theoretical predictions for the vertical (radial) component of the shear-induced mixing D_v in differentially rotating massive stars is roughly three to even ten orders of magnitude stronger than what we constrained here; for several examples refer to Fig. 7 in Talon et al. (1997), Fig. 6 in Meynet & Maeder (2000), Fig. 3 in Mathis et al. (2004), and Figs. 15 and 16 in De-cressin et al. (2009). Based on Eq. (7) in Mathis et al. (2004), D_v depends explicitly on the square of the angular differential rotation frequency $D_v \propto (r d\Omega/dr)^2$. The immediate – and perhaps most plausible – explanation of the low D_{ext} value is that KIC 7760680 is nearly a rigid-body rotator. The range of viable D_{ext} is so negligibly small that neglecting additional mixing in the radiative envelope is justifiable for this star. The extent of the

Table 2

Deduced physical properties of two best asteroseismic models from grid A and B (in Table 1). Uncertainties in grid parameters are set by the minimum stepsize in Table 1, and given in parentheses, which is a lower limit of the true uncertainty. Refer to Figs. 2b and 2c for the extent of each mixing region in both models.

Parameter		
Model Name	mA	mB
Grid	A	B
χ_{red}^2	1808	3647
$M_{\text{ini}} [M_{\odot}]$	3.25 (5)	3.00 (5)
Z_{ini}	0.020 (1)	0.023 (1)
Overshoot	$f_{\text{ov}} = 0.024$ (1)	$\alpha_{\text{ov}} = 0.32$ (1)
$\log D_{\text{ext}} [\text{cm}^2 \text{sec}^{-1}]$	0.75 (25)	0.50 (25)
X_c	0.503 (1)	0.496 (1)
$f_{\text{rot}}^{(\text{opt})} [\text{day}^{-1}]$	0.4805	0.4744
$f_{\text{rot}}^{(\text{opt})} / f_{\text{crit}} [\%]$	26.4	26.6
$M_{\star} [M_{\odot}]$	3.2499	3.0000
$R_{\star} [R_{\odot}]$	2.7895	2.7501
$L_{\star} [L_{\odot}]$	110.8	75.0
Age [10^6 yr]	202	278
$m_{\text{cc}} [M_{\odot}]$	0.6215	0.5437
$r_{\text{cc}} [R_{\odot}]$	0.3356	0.3109
$m_{\text{ov}} [M_{\odot}]$	0.2642	0.2239
$r_{\text{ov}} [R_{\odot}]$	0.0558	0.0495

three mixing regions, in addition to the profile of the hydrogen abundance and the Brunt-Väisälä frequency for the best model are shown in Figs. 2a and 2b.

Fig. 6f shows the position of all evolutionary tracks on the Kiel diagram. The color coding is proportional to $\log \chi_{\text{red}}^2$. The 1σ , 2σ , and 3σ uncertainty boxes are highlighted in grey colour. The position of the best model is flagged with a white circle, which confirms that the asteroseismic parameters of the best model agree with their spectroscopic counterparts; recall that the same agreement was already achieved between $v \sin i$ and the optimised rotation frequency.

That the resulting χ_{red}^2 are larger than one thousand (even for the best models) stems from two facts. First, the relative uncertainties in the mode frequencies σ_i / f_i (see e.g. Fig. 1b or Table 1 in Pápics et al. 2015) are roughly $\sim 10^{-4}$ to 10^{-6} . Second, our current understanding of stellar structure and evolution is based on 1D models, imposing simplifying assumptions (e.g. stellar opacity, stellar composition and mixture, clumpiness in mass loss, treatment of rotation), ignoring some physical processes (e.g. atomic diffusion, radiative levitation, magnetic field), in addition to other physical processes that are not understood well (e.g. the role of internal gravity waves, the angular momentum transport, interaction of various mixing processes). Therefore, it is not surprising that our 1D equilibrium models succeed to explain the overall asteroseismic observables globally, but not in detail.

The distribution of $\log \chi_{\text{red}}^2$ for grid B (with step-function overshoot) is presented in Fig. 7, and the grid parameters are given in Table 1. The $\log \chi_{\text{red}}^2$ values lie in the range $[3.562, 6.825]$. The preferred value for step-function overshoot is $\alpha_{\text{ov}} = 0.31$ to 0.32 . Thus, as with grid A, grid B indicates that sizeable overshoot mixing is required to match the observations. Furthermore, the ex-

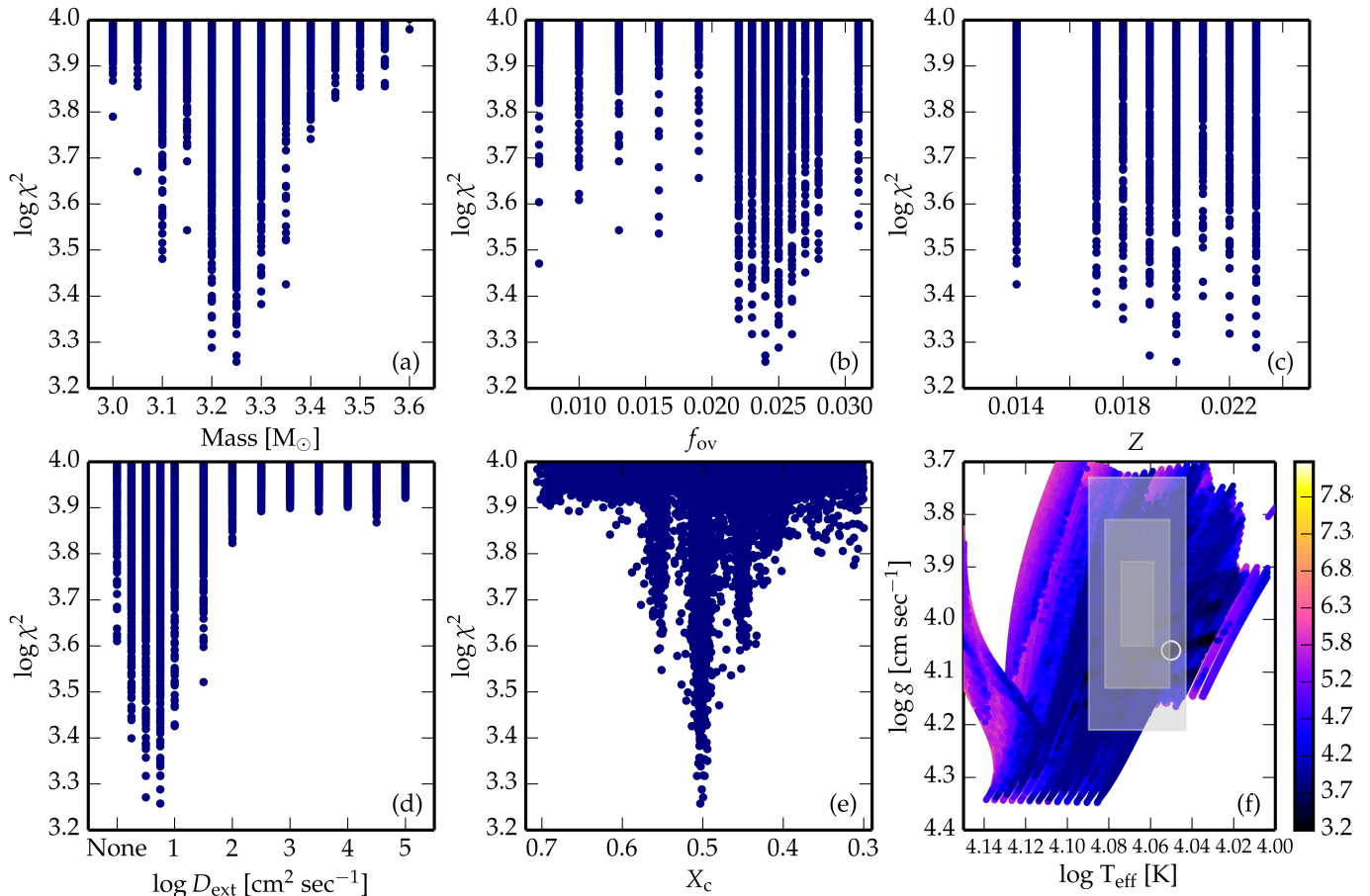


Figure 6. The distribution of the $\log \chi^2_{\text{red}}$ (Eq. 7) for the free parameters of grid A. A similar distribution for grid B is presented in Fig. 7. Panels (a) to (e) show the local minima of $\log \chi^2_{\text{red}}$ versus initial mass M_{ini} , exponential overshoot free parameter f_{ov} , metallicity Z_{ini} , extra diffusive mixing $\log D_{\text{ext}}$, and center hydrogen mass fraction X_c , respectively. For clarity, the ordinate is restricted to models with $\log \chi^2_{\text{red}} \leq 4$. Panel (f) shows the position of the input models on the Kiel diagram. The 1σ , 2σ and 3σ uncertainty boxes for the position of KIC 7760680 from spectroscopy are highlighted as grey boxes. The position of the best model is flagged with a white open circle. The $\log \chi^2_{\text{red}}$ is colour coded.

tra diffusive mixing is also constrained to $\log D_{\text{ext}} = 0.50$ to 0.75 , in excellent agreement with $\log D_{\text{ext}} = 0.75$ found in grid A. In contrast with grid A (Fig. 6), constraining the initial mass, metallicity and age from grid B is less conclusive, and a broader range of values provide equally good overall frequency fits. Fig. 2c shows the mixing property of the best model in grid B.

Fig. 8a shows the resulting period spacing of “the best model” (black filled circles) from mA, compared to the observations (grey symbols, from Fig. 1). The overall fit to the slope of the period spacing is excellent, thanks to the optimised rotation frequency $f_{\text{rot}}^{\text{(opt)}}$. More importantly, the local dips in the observed period spacing are reasonably reproduced, mainly for the shorter-period modes. Towards the longer-period end (with increasing radial order), the quality of the fit noticeably degrades. Fig. 8b shows the relative frequency difference between models and observations $\delta f_i / f_i^{\text{(obs)}}$, where $\delta f_i = f_i^{\text{(obs)}} - f_i^{\text{(mod)}}$. All values are below 1%, so the agreement between observed and theoretical frequencies is at this level. The presence of the strong cyclic pattern in δf_i , among other things, hints at the possible presence of a glitch in Brunt-Väisälä frequency which is not accounted for in our current treatment of the overshooting

mixing. The reason for this, as already elaborated above is the inadequacy of our knowledge about the convective boundary mixing by overshooting, and the missing physics in our 1D models that render the thermal and chemical stratification above the fully mixed core.

The inferred mean rotation frequency for mA is 26.4% of the Roche critical rotation frequency $f_{\text{crit}}^{\text{(Rch)}}$, which is defined as

$$f_{\text{crit}}^{\text{(Rch)}} = \frac{1}{2\pi} \left(\frac{8 G M_{\star}}{27 R_{\star}^3} \right)^{1/2}, \quad (8)$$

where G , M_{\star} and R_{\star} are respectively the gravitational constant, stellar mass and radius – from the best non-rotating 1D model. KIC 7760680 is thus a moderately rotating SPB star. The corresponding estimate of the mean equatorial rotation velocity $v_{\text{eq}} = 2\pi R_{\star} < f_{\text{rot}} > \approx 63 \text{ km sec}^{-1}$, which agrees remarkably with the projected rotation velocity $v \sin i = 62 \pm 5 \text{ km sec}^{-1}$. This means that the inclination angle is $i \approx 80^\circ$, and KIC 7760680 is observed nearly equator on, totally compatible with the detected sectoral ($m \neq 0$) modes.

Previously, we demonstrated that the exponentially decaying overshoot prescription provided a superior frequency fit to the observed modes of Star I (see Table 3

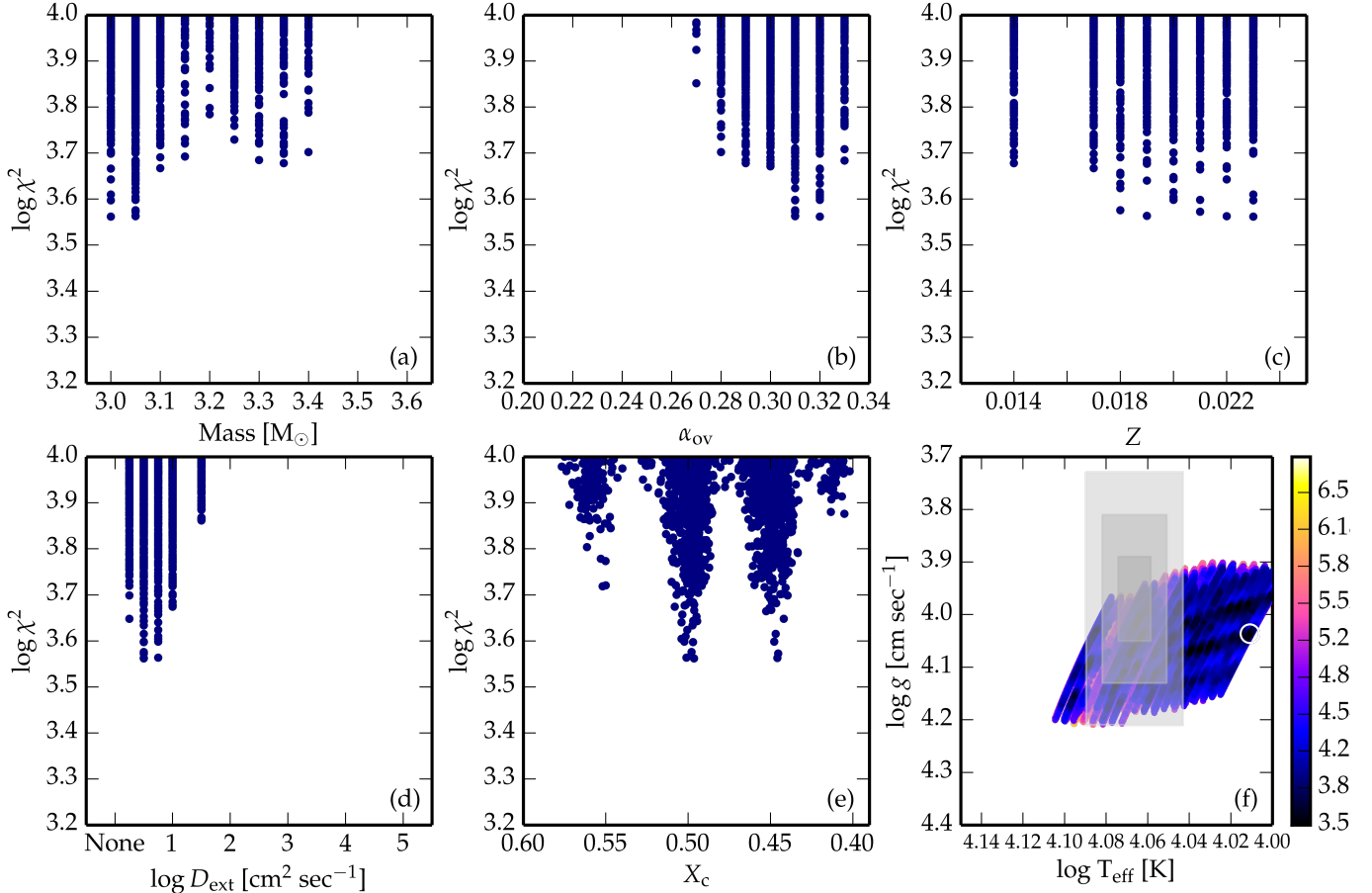


Figure 7. Similar to Fig. 6, but for the grid B with step-function overshooting. The ordinate of the two figures are identical.

in Moravveji et al. 2015). The reason was that the corresponding χ_{red}^2 for the best step-function overshoot model was roughly 2.2 times worse (larger) than that from exponentially-decaying overshoot grid. We repeat the same exercise here, thanks to the extensive Step-Function grid (B) we computed (Table 1). The χ_{red}^2 for the step-function overshoot model from Table 2 is \sim twice the one of the exponential overshoot. This is the second case for which the exponential overshoot prescription is favoured over the classical step-function overshoot.

Table 2 summaries the physical properties of the two best models from grids A and B. Despite different χ_{red}^2 scores, their associated parameters posses interesting similarities, even when adopting two different overshooting prescriptions. The initial mass and metallicity of both models are found reasonably close; the lower-mass model has higher metallicity, and vice versa. This is the well-established $M_{\text{ini}}-Z_{\text{ini}}$ correlation, also shown in Auserloos et al. (2004) for ν Eri, in Briquet et al. (2007) for θ Oph, and in Moravveji et al. (2015) for Star I. The core hydrogen content X_c , and rotation frequency are found to be consistently close in both models. Most importantly, very low extra diffusive mixing D_{ext} is required in both models. Therefore, the global properties of the star, inferred from our seismic modelling, weekly depend on the adopted overshooting model. Regardless of the overshoot prescription option, both models point at a sizeable amount of overshoot, in the presence of rotation. This strengthens our earlier conclusion that moder-

ate rotation requires larger core overshooting, than slow rotation does.

In Table 2, we give the mass contained in the fully mixed convective core m_{cc} , the mass contained in the overshooting region m_{ov} , and their radial extents r_{cc} and r_{ov} , respectively, from the profiles of the equilibrium structure. The relative extent of the overshooting regions in both models (Table 2) are almost identical. The relative overshooting mass with respect to the star mass m_{ov}/M_* in mA (or mB) is 8.1% (or 7.5%). In terms of radial extent, r_{ov}/R_* for the mA (or mB) is 2.0% (or 1.8%). Although, the overshooting region is a narrow part of the star, we show in Sect. 8.3 that many high-order g-modes are perfectly trapped inside this layer. Similarly, we can compare the relative mass and radial extent of the overshooting zone with respect to that of the convective core to shed light on the distance over which the convective eddies travel before losing their identity and falling back. For mA (or mB), $m_{\text{ov}}/m_{\text{cc}}$ is 42.5% (or 41.2%), and similarly $r_{\text{ov}}/r_{\text{cc}}$ is 16.6% (or 15.9%). Therefore, the fully mixed cores in late B-type stars require \sim 16% increase in mass beyond their canonical boundary from the MLT. We argue that future more advanced non-local time-dependent theories of convection (Xiong 1979, 1989; Canuto 2011a,b; Zhang & Li 2012b; Zhang 2013, 2016; Arnett et al. 2015) should closely reproduce our seismic findings. Three dimensional simulations by Browning et al. (2004) for rotating A-type stars already predicted that the convective cores require at least $d_{\text{ov}} \gtrsim 0.20 H_p$

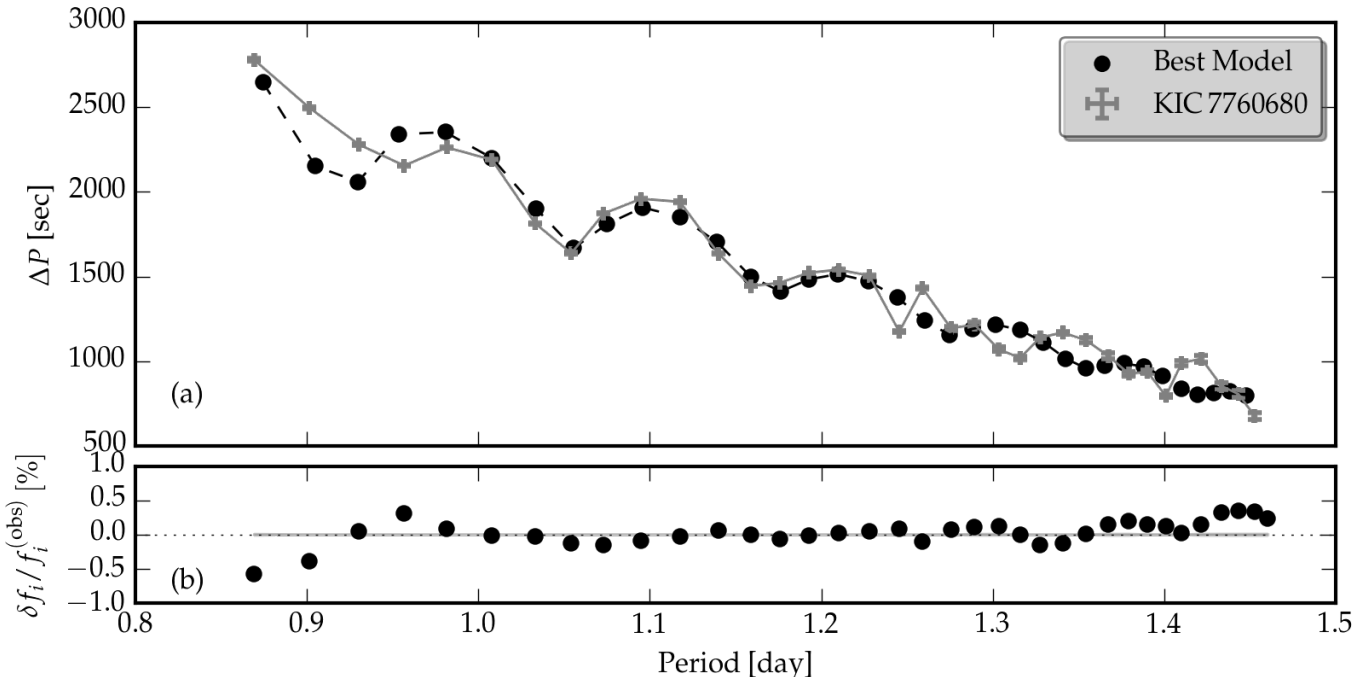


Figure 8. (a) Comparing period spacing from observation (grey) versus best-fit model (black) from grid A. The parameters of this model are given in Table 2. For a comparison with Star I, refer to Fig. 4 in Moravveji et al. (2015). The two patterns reasonably match up to $\sim 1.23 \text{ day}^{-1}$, beyond which the two start to deviate. (b) Percentage of relative frequency difference between the observation and the model, $\delta f_i / f_i^{(obs)}$. The narrow grey area in the middle is the observed 1σ uncertainty shown in Fig. 1b. Note the presence of a cyclic pattern in $\delta f_i / f_i^{(obs)}$.

overshooting extension beyond the canonical boundary, depending on the stiffness (buoyancy jump) of the stratification. The need for such core extension in our results agrees with the predictions of Browning et al.

The relative frequency deviations $\delta f_i / f_i^{(obs)}$ for model mA is below one percent. This is clearly shown in Fig. 8b. For Star I, this was below 0.3 percent, a factor three better than KIC 7760680. Therefore, our seismic models serve as perfect starting point for frequency inversion of the gravity modes, in order to improve the assumed thermal and chemical stratification of the overshooting, beyond the current available models. Although the structure inversion theory for solar-type p-mode pulsators is well established (see Basu 2014; Buldgen et al. 2015, and references therein), no such theory is yet developed for heat-driven high-order g-modes in massive star.

8.2. Nonadiabatic Mode Stability

As an a posteriori test, we consider mode stability properties by computing the non-adiabatic dipole prograde frequencies (Townsend 2005a,b). For the best model, the radial order of the modes that match the observation lie in the range $-53 \leq n_{\text{pg}} \leq -18$. Fig. 9 shows the normalised growth rate $\eta = W / \int_0^{R_*} |dW|$ for the best model, as first introduced by Stellingwerf (1978). Here, W is the total work, from integrating the work integrand dW over the whole star $W = \int_0^{R_*} dW$. Unstable (or stable) modes correspond to positive (or negative) η values, and are shown with filled (or empty) squares. From $\mathcal{N} = 36$ modes, a total of 34 modes are predicted to be unstable, which is in excellent agreement with observations, thanks to employing OP tables with enhanced

Fe and Ni monochromatic opacities. Ignoring the important role of Fe and Ni drastically underestimates the predicted excited modes (Dziembowski & Pamyatnykh 2008; Salmon et al. 2012). Therefore, in addition to solving the β Cep and hybrid pulsating massive stars excitation problem presented in Moravveji (2016), the success in explaining the excitation of the majority of observed modes by incorporating Fe and Ni monochromatic opacity enhancement is another manifestation that the default (OP and OPAL) opacity tables underestimate the Rosseland mean opacity in stellar interiors. Consequently, the stellar interior seems more opaque than believed, and next generation of stellar models should adopt updated tables of Moravveji (2016) and/or Mondet et al. (2015).

In Fig. 9, the period instability domain does not perfectly agree with observations, and seems shifted towards lower-order modes: five short-period g-modes are predicted unstable, but are not observed, in addition to seven long-period g-modes that are observed, but predicted to be stable. We previously found similar issue for Star I; see Fig. 9 in Moravveji et al. (2015).

We speculate that the slight mismatch in Fig. 9 between observed and predicted excited modes can be possibly explained by any of, or the combination of the following three missing physical inputs in the current 1D evolutionary models. (1) Firstly, the gravitational settling and radiative levitation are ignored in our 1D models (due to their ~ 100 times longer computation overhead). The 3D and 1D simulations of Zemska et al. (2014) for a $1.5 M_\odot$ star showed that Fe can gradually accumulate in the iron-bump, modifying the local metallicity, without noticeable change of the surface metallicity. With KIC 7760680 having more than twice the

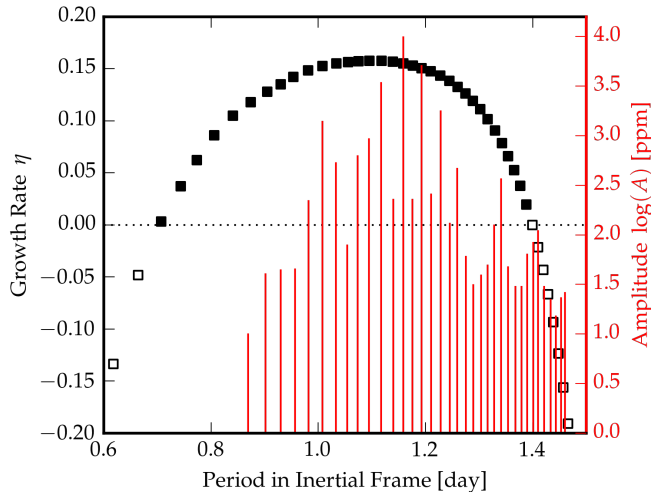


Figure 9. Normalised growth rates η for the best model. The unstable (stable) modes are presented with black filled (empty) squares. The logarithm of the observed mode amplitude A of the dipole series is shown with vertical red lines.

mass contained in the simulations of Zemska et al., the radiative levitation can dominate even further, and contribute very efficiently to iron and nickel accumulation around the iron bump. This important feature is still missing from our MESA models. (2) Secondly, the Fe and Ni are the major contributors to the iron opacity bump, whose abundance in KIC 7760680 are assumed to be solar. This may not necessarily be true. Thus, a slight increase in the Fe and Ni initial abundance (at the cost of slight reduction in initial hydrogen and/or helium) can potentially resolve this problem. This is beyond our current scope, because it calls for re-computing (even a part of) our asteroseismic grid for unknown initial chemical mixtures X_i , for $i = \text{H, He, } \dots, \text{Fe, Ni}$. (3) Thirdly, the iron opacity peak occurs around $\log T \approx 5.2$ to 5.3 dex. We speculate a slight inward shift of the opacity peak towards the hotter interior can help overcoming the radiative damping, and alleviate the lack of sufficient excited modes.

8.3. Mode Trapping in The Deep Stellar Interior

It is instructive to consider the modal behaviour (of our best model) to demonstrate the probing power of high-order g-modes in the deep stellar interior. The rotational kernels $\mathcal{K}_{n,\ell}$, and mode inertia $\mathcal{I}_{n,\ell}$ – which are constructed from the radial and horizontal components of eigendisplacements and defined in Aerts et al. (2010) – are two useful quantities to exploit. The kernels of high-order g-modes become progressively oscillatory by the increase in mode radial order (and mode period), and attain larger amplitude towards the core, compared to the surface. This makes high-order g-modes in rotating SPB stars ideal probes of the near-core environment, provided that the local wavelength of the mode is roughly equal to or smaller than the length scale of the change of structure in the background model (Cumha et al. 2015; Belyaev et al. 2015). In such cases, the model g-modes are able to *resolve* the structure of their background medium (which they propagate in), and their frequencies reveal the shortcomings in treating the near-core thermal and chemical stratification, by deviating from observations. We argue that a subset of g-modes in KIC 7760680 are trapped in-

side the overshooting region, and reveal that the current state of the modelling of chemical mixing and thermal stratification in that region are not accurate enough to explain the high precision data.

The two panels in Fig. 10 compare several seismic properties of the lowest-order g-mode $n_{\text{pg}} = -18$ (left), and the highest-order one $n_{\text{pg}} = -53$ (right) in the best model. They represent the two extreme mode behaviours in the observed series, while those of the intermediate modes exhibit a smooth transition between the two shown here. The top panels show the period spacing (filled dots) and mode inertia (empty dots) versus mode periods. The bottom panels show the profile of normalised rotational kernels $K_{n,\ell}$; in this panel, the convective zone is highlighted in blue, and the Brunt-Väisälä frequency is shown with a dashed red line.

The kernels exhibit two significant features on top of the convective core: (a) Both modes exhibit partial trapping in the μ -gradient region – associated with the broad bump in the Brunt-Väisälä frequency. The kernels of the modes associated with the dips in the period spacing attain highest relative amplitude in the μ -gradient region, and become fully trapped. (b) The kernels of the modes with radial order exceeding ~ 30 , i.e. $n_{\text{pg}} \lesssim -30$, exhibit an additional trapping in the overshooting region between the boundary of the convective core, and the base of the bump in the Brunt-Väisälä frequency. Notice the final emergence of a fully-trapped mode in the bottom left panel in Fig. 10, at the mass coordinate $m \approx 0.75 M_{\odot}$. The highest-order modes which exhibit this additional trapping are those which probe the overshooting zone, and provide very precise diagnostic of the physical structure of this region.

Consequently, the entire series of identified g-modes of KIC 7760680 allow exploiting the extent and physical conditions of chemically homogeneous (overshooting) and inhomogeneous (μ -gradient) layers in massive stars. The success (or failure) in matching the individual observed frequencies is a reward (or penalty) of the accuracy of our current understanding and implementation of the physics of stellar interior. The fact that lower-order modes ($n_{\text{pg}} \gtrsim -30$) better match the observation is a clear evidence that the structure of the μ -gradient layer is well represented in our 1D evolutionary model. However, the evident period spacing deviations of higher order modes ($n_{\text{pg}} \lesssim -30$) from observations unambiguously indicates a lack of missing physics of the overshoot mixing. This explains the cyclic deviations between frequencies of the best model from observations presented in Fig. 8b. This can be attributed to the ad-hoc implementation of overshoot (e.g. Sect. 3) in one-dimensional models, since our local, time-averaged description of convective mixing by MLT does not consistently account for convection-induced mixing beyond the core boundaries (e.g. Browning et al. 2004; Arnett 2014, and references therein).

The non-local, time-dependent convective models (see e.g. Xiong 1979, 1989; Canuto 2011a,b; Zhang & Li 2012b; Zhang 2013, 2016; Arnett et al. 2015; Pasetto et al. 2014, 2015) may be able to provide better insight into the physical structure of the overshoot region, and allow improving the fit to the observed period spacing of g-mode pulsators. Therefore, the long series of dipole period spacing in KIC 7760680 and Star I provide two ideal

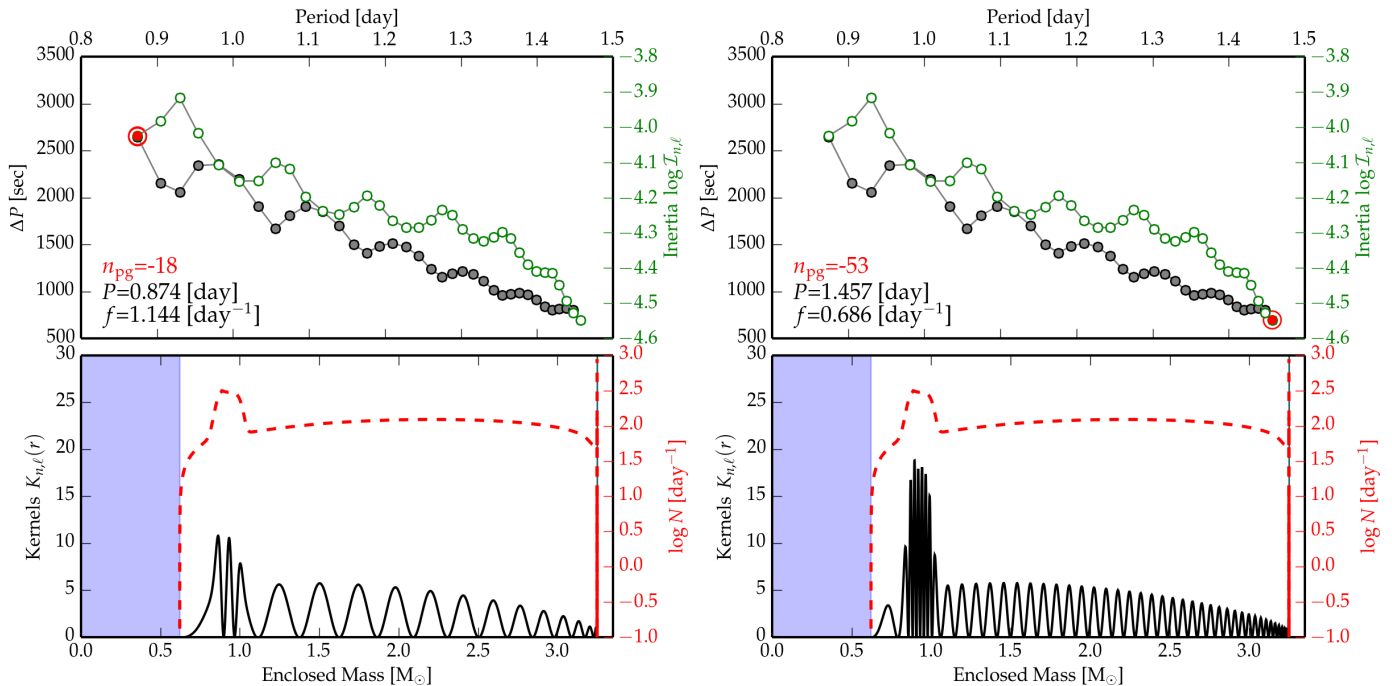


Figure 10. The mode Kernels $\mathcal{K}_{n,\ell}$ (bottom solid line) and the logarithm of mode inertia $\mathcal{I}_{n,\ell}$ (top empty dots) for the shortest-period mode with period $P_1 = 0.873 \text{ d}^{-1}$ (left), and for the longest-period mode with period $P_{36} = 1.457 \text{ d}^{-1}$ (right). On the top panels, the period spacing is shown in grey filled dots. The red empty circles mark the corresponding mode. On the bottom panels, the blue area shows the convective core where g-modes are evanescent, and the red dashed line shows the Brunt-Väisälä frequency $\log N$. The best model from Table 2 is used as the input.

tests for theories of convective and non-convective heat, chemical and angular momentum transport.

9. SUMMARY, DISCUSSION AND CONCLUSION

Let us revisit and discuss the four questions raised in Sect. 1. In this paper, we carried out a thorough forward seismic modelling of KIC 7760680, the richest SPB star discovered so far. We computed two non-rotating MESA grids, and incorporated the effect of rotation on g-modes by employing the traditional approximation. The unknown equatorial rotation frequency of the target was varied and optimized by enforcing to match the exact number of dipole prograde modes within the observed range; this approach, automatically reproduces the negative slope in the observed period spacing. All models in our grids were ranked by a χ^2_{red} merit function that accounted for fitting of the frequencies. We showed that KIC 7760680 is a $3.25 M_{\odot}$ SPB star that rotates at $\sim 26\%$ its Roche breakup frequency. At this moderate rotation velocity, substantial overshooting is required to match the frequencies. Therefore, we demonstrate that rotation increases convective overshooting from the core, compared to the non-rotating case.

Considering Star I, we managed to tightly constrain f_{ov} to ~ 0.017 , and favored the exponential prescription over the step-function. It is noteworthy that the diffusive exponential prescription is also supported by the time-dependent convection model of Zhang (2013), Zhang & Li (2012a), and Zhang (2016) (and the references therein), which contradicts with the predictions of Zahn (1991) and Viallet et al. (2015) that core overshooting results into an adiabatic extension of the core. Our seismically derived overshoot value for the best models are $f_{\text{ov}} = 0.024$ and $\alpha_{\text{ov}} = 0.32$. They are in excellent

agreement with the previous studies (reviewed by Aerts 2013, and the references therein), in addition to those of Stancliffe et al. (2015) from fitting the global observables of nine binary systems, between 1.3 and $6.2 M_{\odot}$, and the seismic modelling of Deheuvels et al. (2016) for F stars at the onset of having convective cores. Thus, a global picture on the overshoot mixing for a broad range of stellar masses is gradually emerging.

We allowed substantial mixing in the radiative regions as we chose to vary D_{ext} from zero up to 10^5 . We found at least an order of magnitude smaller values, compared to the theoretical predictions of Mathis et al. (2004). In case shear-induced turbulent mixing were important in KIC 7760680, then our seismic models – through their χ^2_{red} scores – should have preferred higher values for $\log D_{\text{ext}}$. From Fig. 6d, this is obviously not the case. Since the shear-induced mixing depends explicitly on the gradient of angular velocity, we infer that such gradient is small, if not zero, and the upper limit of the resulting effective diffusion transport coefficient is roughly $D_{\text{ext}} \lesssim 10$. The absence of differential rotational, and shear-induced mixing is a strong evidence that KIC 7760680 is most probably rotating rigidly. This is quite acceptable in the light of finding small shear discovered in two *Kepler* F-type stars (Kurtz et al. 2014; Saio et al. 2015). In fact, heat-driven g-modes (Lee & Saio 1993) and stochastically excited internal gravity waves (Rogers 2015) are predicted to efficiently redistribute angular momentum inside B-type stars, and induce near-rigid rotation. KIC 7760680 could be another manifestation of this. In the meanwhile, we cannot exclude other possible mechanisms that can suppress mixing, and enforce rigid body rotation. In the light of recent advancements in asteroseismology, deep-

rooted fossil magnetic fields turn out to be ubiquitous in intermediate main sequence stars (Stello et al. 2016), and their red giant descendants (Fuller et al. 2015). Asteroseismic modelling of the the magnetic β Cep pulsator V 2052 Ophiuchi by Briquet et al. (2012) revealed that an internal magnetic field can suppress core overshooting. In addition, Briquet et al. (2016) showed that the weakly magnetic B2 IV-V SPB star ζ Cas rotates rigidly, with a magnetic field of strength 100–150 G inhibiting mixing in its envelope. The observed nitrogen enhancement was then attributed to the transport by internal gravity waves. Because KIC 7760680 is an intermediate mass star, it can be a showcase of magnetic inhibition of chemical mixing by rigid rotation.

We inferred (in Sect. 8.1) that KIC 7760680 is nearly a solid body rotator, because the extra diffusive mixing is limited to $\log D_{\text{ext}} \approx 0.75$. This is not surprising. The two γ Dor stars (which are similarly high-order low-degree g-mode pulsators with roughly half the mass of KIC 7760680) studied by Kurtz et al. (2014) and Saio et al. (2015) unambiguously exhibit core-to-surface rotation frequency close to unity, from the frequency splittings of their p- and g-modes. Star I was also shown to be a very slowly rotating star with a counter rotating envelope with respect to its core (Triana et al. 2015). Rogers (2015) successfully explained all these observed cases through very efficient angular momentum transport carried by internal gravity waves (see also Zahn et al. 1997; Talon & Charbonnel 2005; Rogers et al. 2013). The same mechanism is used by Aerts & Rogers (2015) to explain the observed background power excess in the periodograms of three CoRoT O-type dwarfs. Therefore, in dwarf stars earlier than A-type, the angular momentum transport can be more efficient than predicted, and it can impose near-rigid envelope rotation.

The two recently modelled *Kepler* SPB stars, Star I and KIC 7760680 are the best understood stars of their class. Their constrained physical parameters can serve as starting point for more sophisticated and/or realistic theories of energy and chemical transport by turbulent convection, beyond MLT. In fact, more realistic future convection models should succeed to improve fitting the observed frequencies of these two SPB stars, in addition to surviving the helioseismic tests.

The authors are grateful to Peter I. Pápics for the reanalysis of the light curve, and to determine the correction factor to be applied for frequency uncertainties ($Q = 4.0$) compared to those derived from NLLS. The research leading to these results has received funding from the People Programme (Marie Curie Actions) of the European Union’s Seventh Framework Programme FP7/2007-2013/ under REA grant agreement N° 623303 (ASAMBA), from the European Research Council (ERC) under the European Union’s Horizon 2020 research and innovation programme grant N° 670519 (MAMSIE), and from the European Community’s Seventh Framework Programme FP7-SPACE-2011-1, project N° 312844 (SPACEINN). RHDT acknowledges support from NSF under the SI² program grants (ACI-1339600) and NASA under the TCAN program grants (NNX14AB55G). SM acknowledges funding by the ERC grant N° 647383 (SPIRE). The compu-

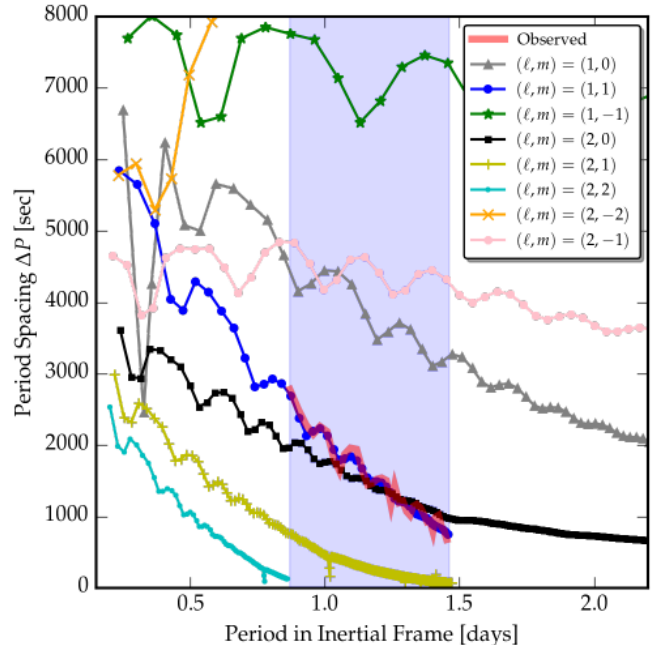


Figure 11. Period spacing ΔP for eight combinations of (ℓ, m) for dipole and quadrupole modes, compared with the observed series (red solid line). The input model is set to $\sim 24\%$ rotation frequency with respect to $J_{\text{rot}}^{(\text{Rch})}$.

tational resources and services used in this work were provided by the VSC (Flemish Supercomputer Center), funded by the Hercules Foundation and the Flemish Government - department EWI.

APPENDIX

DISTINGUISHING HARMONIC DEGREE AND AZIMUTHAL ORDER

Fig. 11 shows eight period spacing series for dipole and quadrupole modes using TAR. The input model fulfils the position of the star on the Kiel diagram, and is set to uniform rotation with 24.2% with respect to Roche critical frequency (Eq. 8). The observed ΔP pattern (red line) is well reproduced by dipole prograde modes, while all other spacings fail to satisfy Eq. 5, and match the slope of the period spacing. Moreover, extremely high radial orders of up to $|n_{\text{pg}}| \approx 700$ were needed for $(\ell, m) = (2, 1)$ and $(2, 2)$ to force them towards the observed range, which contradicts with the requirement $\mathcal{N} = 36$. Thus, the observed serie in Fig. 1a is identified as dipole prograde $(\ell, m) = (1, +1)$ g-modes.

DELIVERABLES, INLISTS AND OPACITY TABLES

Following the MESA users’ code of conduct stated in Paxton et al. (2011), we publish the MESA and GYRE inlists, and the structure file of the best asteroseismic model of KIC 7760680 (compatible with GYRE). This ensures the reproducibility of our results, provided similar MESA and GYRE versions are used. These products are available through the following static link: <https://fys.kuleuven.be/ster/Projects/ASAMBA>. The adopted OP opacity tables are already available from https://bitbucket.org/ehsan_moravveji/op-mono.

ITERATIVE PROCEDURE TO OPTIMIZE F_{ROT}

Here, we explain the iterative procedure to optimise f_{rot} (or equivalently η_{rot}) using Eqs. (4) and (5). Fig. 12 illustrates the procedure. The first attempt corresponds to a small trial f_{rot} , and the second one corresponds to a much larger trial value for f_{rot} , ensuring a change of sign of $d\mathcal{N}$. For the third attempt, we estimate f_{rot} by Newton-Raphson root-finding, assuming a line connecting the first two points. From the fourth attempt onward, we use the Van Wijngaarden-Dekker-Brent (Brent 1973) root-finding algorithm to locate the zero of $d\mathcal{N}$ (see also Press et al. 2007). The iterations proceed, until the root is successfully located. Considering the fact that $d\mathcal{N}$ is an integer-valued function, it seldom happens that a tiny change in f_{rot} proposed by the previous (Brent) guess does not change \mathcal{M} . In such cases $d\mathcal{N}$ is zero (has a staircase shape), and the Brent scheme diverges. To avoid such circumstances, we employ an iterative Bisection method (Press et al. 2007) to converge to the root of $d\mathcal{N}$. During all these attempts, we call GYRE, and store the intermediate results on the disk, until the procedure succeeds. Finally, we store the optimal rotation frequency $f_{\text{rot}}^{(\text{opt})}$ as an additional attribute in the GYRE output summary file.

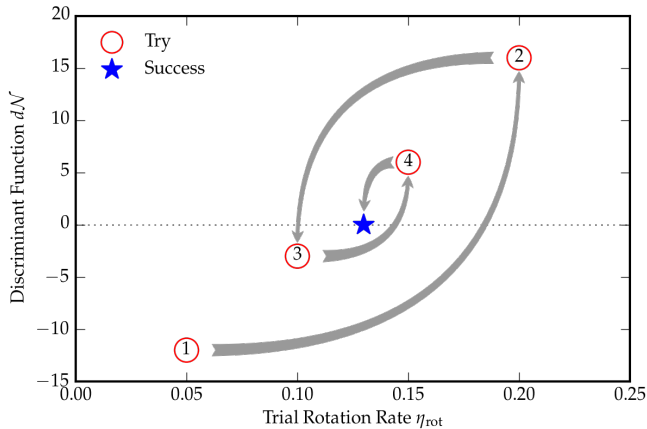


Figure 12. The scheme for optimizing $\eta_{\text{rot}} = f_{\text{rot}}/f_{\text{rot}}^{(\text{Rch})}$.

REFERENCES

- Aerts, C. 2013, in EAS Publications Series, Vol. 64, EAS Publications Series, 323–330
- Aerts, C., Christensen-Dalsgaard, J., & Kurtz, D. W. 2010, *Asteroseismology*, Astronomy and Astrophysics Library, Springer Berlin Heidelberg
- Aerts, C., Lamers, H. J. G. L. M., & Molenberghs, G. 2004, *A&A*, 418, 639
- Aerts, C., & Rogers, T. M. 2015, *ApJL*, 806, L33
- Aprilia, Lee, U., & Saio, H. 2011, *MNRAS*, 412, 2265
- Arnett, W. D. 2014, in *New Windows on Massive Stars: Asteroseismology, Interferometry and Spectropolarimetry*, ed. G. Meynet, C. Georgy, J. Groh, & P. Stee (Cambridge University Press)
- Arnett, W. D., Meakin, C., Viallet, M., et al. 2015, *The Astrophysical Journal*, 809, 30
- Asplund, M., Grevesse, N., Sauval, A. J., & Scott, P. 2009, *ARA&A*, 47, 481
- Ausseloos, M., Scuflaire, R., Thoul, A., & Aerts, C. 2004, *MNRAS*, 355, 352
- Badnell, N. R., Bautista, M. A., Butler, K., et al. 2005, *MNRAS*, 360, 458
- Bailey, J. E., Nagayama, T., Loisel, G. P., et al. 2015, *Nature*, 517, 56
- Ballot, J., Lignières, F., Prat, V., Reese, D. R., & Rieutord, M. 2012, in *Astronomical Society of the Pacific Conference Series*, Vol. 462, *Progress in Solar/Stellar Physics with Helio- and Asteroseismology*, ed. H. Shibahashi, M. Takata, & A. E. Lynas-Gray, 389
- Ballot, J., Lignières, F., Reese, D. R., & Rieutord, M. 2010, *A&A*, 518, A30
- Balona, L. A., Pigulski, A., Cat, P. D., et al. 2011, *MNRAS*, 413, 2403
- Basu, S. 2014, *Studying stars through frequency inversions*, ed. P. L. Pallé & C. Esteban, 87
- Belyaev, M. A., Quataert, E., & Fuller, J. 2015, *MNRAS*, 452, 2700
- Böhm-Vitense, E. 1958, *ZAp*, 46, 108
- Bouabid, M.-P., Dupret, M.-A., Salmon, S., et al. 2013, *MNRAS*, 429, 2500
- Brent, R. P. 1973, *Algorithms for minimization without derivatives*, Prentice-Hall series in automatic computation (Englewood Cliffs, N.J. Prentice-Hall)
- Briquet, M., Morel, T., Thoul, A., et al. 2007, *MNRAS*, 381, 1482
- Briquet, M., Neiner, C., Petit, P., et al. 2016, *A&A*, 587, A126
- Briquet, M., Neiner, C., Aerts, C., et al. 2012, *MNRAS*, 427, 483
- Browning, M. K., Brun, A. S., & Toomre, J. 2004, *ApJ*, 601, 512
- Buldgen, G., Reese, D. R., & Dupret, M. A. 2015, *A&A*, 583, A62
- Canuto, V. M. 2011a, *A&A*, 528, A76
- . 2011b, *A&A*, 528, A80
- Castelli, F., & Kurucz, R. L. 2003, in *IAU Symposium*, Vol. 210, *Modelling of Stellar Atmospheres*, ed. N. Piskunov, W. W. Weiss, & D. F. Gray, A20
- Cox, J. P., & Giuli, R. T. 1968, *Principles of stellar structure*, ed. Cox, J. P. & Giuli, R. T.
- Cunha, M. S., Stello, D., Avelino, P. P., Christensen-Dalsgaard, J., & Townsend, R. H. D. 2015, *ApJ*, 805, 127
- De Cat, P., & Aerts, C. 2002, *A&A*, 393, 965
- Decressin, T., Mathis, S., Palacios, A., et al. 2009, *A&A*, 495, 271
- Degroote, P., Briquet, M., Catala, C., et al. 2009, *A&A*, 506, 111
- Deheuvels, S., Brandão, I., Silva Aguirre, V., et al. 2016, *arXiv:1603.02332*
- Dintrans, B., & Rieutord, M. 2000, *A&A*, 354, 86
- Dufton, P. L., Langer, N., Dunstall, P. R., et al. 2013, *A&A*, 550, A109
- Dziembowski, W. A., & Goode, P. R. 1992, *ApJ*, 394, 670
- Dziembowski, W. A., Moskalik, P., & Pamyatnykh, A. A. 1993, *MNRAS*, 265, 588
- Dziembowski, W. A., & Pamyatnykh, A. A. 1991, *A&A*, 248, L11
- . 2008, *MNRAS*, 385, 2061
- Eckart, C. 1960, *Hydrodynamics of Oceans and Atmospheres*, Pergamon Press, Oxford
- Endal, A. S., & Sofia, S. 1976, *ApJ*, 210, 184
- . 1978, *ApJ*, 220, 279
- Espinosa Lara, F., & Rieutord, M. 2013, *A&A*, 552, A35
- Freytag, B., Ludwig, H.-G., & Steffen, M. 1996, *A&A*, 313, 497
- Fuller, J., Cantiello, M., Stello, D., Garcia, R. A., & Bildsten, L. 2015, *Science*, 350, 423
- Gautschy, A., & Saio, H. 1993, *MNRAS*, 262, 213
- Heger, A., Langer, N., & Woosley, S. E. 2000, *ApJ*, 528, 368
- Heger, A., Woosley, S. E., & Spruit, H. C. 2005, *ApJ*, 626, 350
- Herwig, F. 2000, *A&A*, 360, 952
- Huang, W., Gies, D. R., & McSwain, M. V. 2010, *ApJ*, 722, 605
- Huat, A.-L., Hubert, A.-M., Baudin, F., et al. 2009, *A&A*, 506, 95
- Kippenhahn, R., & Thomas, H.-C. 1970, in *IAU Colloq. 4: Stellar Rotation*, ed. A. Slettebak, 20
- Kurtz, D. W., Saio, H., Takata, M., et al. 2014, *MNRAS*, 444, 102
- Langer, N., El Eid, M. F., & Fricke, K. J. 1985, *A&A*, 145, 179
- Ledoux, P. 1951, *ApJ*, 114, 373
- Lee, U., Mathis, S., & Neiner, C. 2016, *MNRAS*, 457, 2445
- Lee, U., Neiner, C., & Mathis, S. 2014, *MNRAS*, 443, 1515
- Lee, U., & Saio, H. 1986, *MNRAS*, 221, 365
- . 1993, *MNRAS*, 261, 415
- Lee, U., & Saio, H. 1997, *The Astrophysical Journal*, 491, 839
- Maeder, A. 1975, *A&A*, 40, 303
- . 2009, *Physics, Formation and Evolution of Rotating Stars*, ed. Maeder, A., doi:10.1007/978-3-540-76949-1
- Maeder, A., Meynet, G., Lagarde, N., & Charbonnel, C. 2013, *A&A*, 553, A1

- Maeder, A., & Zahn, J.-P. 1998, *A&A*, 334, 1000
- Mathis, S. 2013, *Studying Stellar Rotation and Convection: Theoretical Background and Seismic Diagnostics*, ed. M. Goupil, K. Belkacem, C. Neiner, F. Lignières, & J. J. Green (Berlin, Heidelberg: Springer Berlin Heidelberg), 23–47
- Mathis, S., Neiner, C., & Tran Minh, N. 2014, *A&A*, 565, A47
- Mathis, S., Palacios, A., & Zahn, J.-P. 2004, *A&A*, 425, 243
- Mathis, S., Talon, S., Pantillon, F.-P., & Zahn, J.-P. 2008, *Sol. Phys.*, 251, 101
- Mathis, S., & Zahn, J.-P. 2004, *A&A*, 425, 229
- 2005, *A&A*, 440, 653
- Meynet, G., & Maeder, A. 2000, *A&A*, 361, 101
- Miglio, A., Montalbán, J., Noels, A., & Eggenberger, P. 2008, *MNRAS*, 386, 1487
- Mondet, G., Blancard, C., Cossé, P., & Faussurier, G. 2015, *ApJS*, 220, 2
- Moravveji, E. 2015, in *EAS Publications Series*, Vol. 71, *EAS Publications Series*, 317–320
- Moravveji, E. 2016, *MNRAS*, 455, L67
- Moravveji, E., Aerts, C., Pápics, P. I., Triana, S. A., & Vandoren, B. 2015, *A&A*, 580, A27
- Nagayama, T., Bailey, J. E., Loisel, G., et al. 2016, *Phys. Rev. E*, 93, 023202
- Neiner, C., Floquet, M., Samadi, R., et al. 2012, *A&A*, 546, A47
- Nieva, M.-F., & Przybilla, N. 2012, *A&A*, 539, A143
- Pamyatnykh, A. A. 1999, *Acta Astron.*, 49, 119
- Pantillon, F. P., Talon, S., & Charbonnel, C. 2007, *A&A*, 474, 155
- Pápics, P. I., Moravveji, E., Aerts, C., et al. 2014, *A&A*, 570, A8
- Pápics, P. I., Tkachenko, A., Aerts, C., et al. 2015, *ApJL*, 803, L25
- Pápics, P. I., Briquet, M., Auvergne, M., et al. 2011, *A&A*, 528, A123+
- Pápics, P. I., Briquet, M., Baglin, A., et al. 2012, *A&A*, 542, A55
- Pasetto, S., Chiosi, C., Chiosi, E., Cropper, M., & Weiss, A. 2015, *arXiv:1511.08811*
- Pasetto, S., Chiosi, C., Cropper, M., & Grebel, E. K. 2014, *MNRAS*, 445, 3592
- Paxton, B., Bildsten, L., Dotter, A., et al. 2011, *ApJS*, 192, 3
- Paxton, B., Cantiello, M., Arras, P., et al. 2013, *ApJS*, 208, 4
- Paxton, B., Marchant, P., Schwab, J., et al. 2015, *ApJS*, 220, 15
- Prat, V., Lignières, F., & Ballot, J. 2016, *A&A*, 587, A110
- Press, W. H., Teukolsky, S. A., Vetterling, W. T., & Flannery, B. P. 2007, *Numerical Recipes 3rd Edition: The Art of Scientific Computing*, 3rd edn. (New York, NY, USA: Cambridge University Press)
- Puls, J., Sundqvist, J. O., & Markova, N. 2015, in *IAU Symposium*, Vol. 307, *IAU Symposium*, ed. G. Meynet, C. Georgy, J. Groh, & P. Stee, 25–36
- Ramírez-Agudelo, O. H., Simón-Díaz, S., Sana, H., et al. 2013, *A&A*, 560, A29
- Ramírez-Agudelo, O. H., Sana, H., de Mink, S. E., et al. 2015, *A&A*, 580, A92
- Raskin, G., van Winckel, H., Hensberge, H., et al. 2011, *A&A*, 526, A69
- Reese, D., Lignières, F., & Rieutord, M. 2006, *A&A*, 455, 621
- Rogers, T. M. 2015, *ApJL*, 815, L30
- Rogers, T. M., Lin, D. N. C., McElwaine, J. N., & Lau, H. H. B. 2013, *ApJ*, 772, 21
- Roxburgh, I. W. 1965, *MNRAS*, 130, 223
- Saio, H., & Deupree, R. G. 2012, in *Astronomical Society of the Pacific Conference Series*, Vol. 462, *Progress in Solar/Stellar Physics with Helio- and Asteroseismology*, ed. H. Shibahashi, M. Takata, & A. E. Lynas-Gray, 398
- Saio, H., Kurtz, D. W., Takata, M., et al. 2015, *MNRAS*, 447, 3264
- Salmon, S., Montalbán, J., Morel, T., et al. 2012, *MNRAS*, 422, 3460
- Savonije, G. J. 2005, *A&A*, 443, 557
- 2013, *A&A*, 559, A25
- Schwarzenberg-Czerny, A. 1991, *MNRAS*, 253, 198
- Seaton, M. J. 2005, *MNRAS*, 362, L1
- Shibahashi, H., & Ishimatsu, H. 2013, in *Astrophysics and Space Science Proceedings*, Vol. 31, *Stellar Pulsations: Impact of New Instrumentation and New Insights*, ed. J. C. Suárez, R. Garrido, L. A. Balona, & J. Christensen-Dalsgaard, 49
- Soufi, F., Goupil, M. J., & Dziembowski, W. A. 1998, *A&A*, 334, 911
- Stanciliffe, R. J., Fossati, L., Passy, J.-C., & Schneider, F. R. N. 2015, *A&A*, 575, A117
- Stellingwerf, R. F. 1978, *AJ*, 83, 1184
- Stello, D., Cantiello, M., Fuller, J., et al. 2016, *Nature*, 529, 364
- Talon, S., & Charbonnel, C. 2005, *A&A*, 440, 981
- Talon, S., Zahn, J.-P., Maeder, A., & Meynet, G. 1997, *A&A*, 322, 209
- Tassoul, M. 1980, *ApJS*, 43, 469
- Townsend, R. H. D. 2003a, *MNRAS*, 343, 125
- 2003b, *MNRAS*, 340, 1020
- 2005a, *MNRAS*, 360, 465
- 2005b, *MNRAS*, 364, 573
- Townsend, R. H. D., & Teitler, S. A. 2013, *MNRAS*, 435, 3406
- Triana, S. A., Moravveji, E., Pápics, P. I., et al. 2015, *ApJ*, 810, 16
- Unno, W., Osaki, Y., Ando, H., Saio, H., & Shibahashi, H. 1989, *Nonradial oscillations of stars*, ed. Unno, W., Osaki, Y., Ando, H., Saio, H., & Shibahashi, H.
- Van Reeth, T., Tkachenko, A., Aerts, C., et al. 2015a, *A&A*, 574, A17
- 2015b, *ApJS*, 218, 27
- Viallet, M., Meakin, C., Prat, V., & Arnett, D. 2015, *A&A*, 580, A61
- Vink, J. S., de Koter, A., & Lamers, H. J. G. L. M. 2001, *A&A*, 369, 574
- Waelkens, C. 1991, *A&A*, 246, 453
- Waelkens, C., Aerts, C., Kestens, E., Grenon, M., & Eyer, L. 1998, *A&A*, 330, 215
- Xiong, D.-R. 1979, *Acta Astronomica Sinica*, 20, 238
- 1989, *A&A*, 213, 176
- Zahn, J.-P. 1991, *A&A*, 252, 179
- 1992, *A&A*, 265, 115
- Zahn, J.-P., Talon, S., & Matias, J. 1997, *A&A*, 322, 320
- Zemskova, V., Garaud, P., Deal, M., & Vauclair, S. 2014, *ApJ*, 795, 118
- Zhang, Q. S. 2013, *ApJS*, 205, 18
- 2016, *ApJ*, 818, 146
- Zhang, Q. S., & Li, Y. 2012a, *ApJ*, 746, 50
- 2012b, *ApJ*, 750, 11